# Satellite-based Near-Real-Time Global Daily Terrestrial Evapotranspiration Estimates

Lei Huang[1*], Yong Luo[1*], Jing M. Chen[2,3], Qiuhong Tang[4,5], Tammo Steenhuis[6], Wei Cheng[7] and Wen Shi[1]

[1]Department of Earth System Science, Ministry of Education Key Laboratory for Earth System Modeling, Institute for Global Change Studies, Tsinghua University, Beijing 100084, China
[2]Key Laboratory for Humid Subtropical Ecogeographical Processes of the Ministry of Education, School of Geographical Sciences, Fujian Normal University, Fuzhou, 350007, China
[3]Department of Geography and Planning, University of Toronto, Ontario, M5S 3G3, ON, Canada
[4]Key Laboratory of Water Cycle and Related Land Surface Processes, Institute of Geographic Sciences and Natural Resources Research, Chinese Academy of Sciences, Beijing 100101, China
[5]University of Chinese Academy of Sciences, Beijing 101408, China
[6]Department of Biological and Environmental Engineering, Cornell University, Ithaca 14850, New York, USA
[7]Key Laboratory of Land Surface Pattern and Simulation, Institute of Geographic Sciences and Natural Resources Research, Chinese Academy of Sciences, Beijing 100101, China

*Correspondence to* Lei Huang (leihuang007@mail.tsinghua.edu.cn) or
Yong Luo (Yongluo@mail.tsinghua.edu.cn)

**Abstract.**

Accurate and timely information on global terrestrial actual evapotranspiration (ET) is crucial in agriculture, water resource management and drought forecasting in a changing climate. While numerous satellite-based ET products have been developed in recent decades, few provide near-real-time global terrestrial ET estimates. The MOD16 ET dataset, currently updating at the fastest rate, still experiences a delay of over two weeks. This is because most satellite-based ET algorithms rely on meteorological data from land surface models or in situ measurements, which cannot be obtained in near-real-time, resulting in delays of more than two weeks. To expedite global ET data access, we developed the Moderate Resolution Imaging Spectroradiometer (MODIS) based Variation of Standard Evapotranspiration Algorithm (VISEA) to provide global daily ET data within a week of the actual measurements at a spatial resolution of 0.05°. The VISEA model incorporates several key components: (1) A vegetation index (VI)-temperature (Ts) triangle method to simulate air temperature (Ta), serves as a basis for calculating other meteorological parameters (e.g., water vapor deficit and wind speed); (2) A daily evaporation fraction (EF) method based on the decoupling parameter, converts satellite-based instantaneous observations into daily ET estimates; (3) A net radiation calculation program takes into account cloud coverage in the atmosphere's downward longwave radiation. The VISEA model is driven by shortwave radiation from the European Centre for Medium-range Weather Forecasts (ERA5-Land) and MODIS land products, e.g., surface reflectance, land surface temperature/emissivity, land cover products~~)~~, vegetation indices, and albedo as inputs. To assess its accuracy, we compared VISEA with measurements from 149 flux towers, five other satellite-based global ET products, and precipitation data from the Global Precipitation Climatology Centre (GPCC). The evaluations show that the near-real-time ET using VISEA performs with similar accuracy to other existing data products and offers a significantly shorter time frame for daily data availability. Over 12 landcover types, the mean R is about 0.6 with an RMSE of 1.4 mm day$^{-1}$ at a daily scale. Furthermore, the consistent spatial patterns of multi-year average

VISEA align closely with GPCC precipitation data, reaffirming the dataset's ability to accurately represent global terrestrial ET distribution. To emphasize the capabilities of the VISEA for drought monitoring, we analyzed the spatial and temporal variations of ET during a drought event and subsequent recovery with precipitation in the Yangtze River basin from August ~~28th~~26th to September ~~1st~~2nd, 2022. The VISEA distinctly illustrated low mean ET levels (<0.~~2~~5 mm day$^{-1}$) across~~ most areas of~~ the Yangtze River Basin on August 28th, indicating the severity of the drought. Conversely, a noticeable increase in ET (>~~0.9~~1 mm day$^{-1}$) is observed on August ~~29th~~30th, signifying the retreat of the drought due to precipitation. The near-real-time global daily terrestrial ET estimates could be valuable for meteorology and hydrology applications requiring real-time data, particularly in coordinating relief efforts during droughts. The VISEA code and dataset are available at https://doi.org/10.11888/Terre.tpdc.300782 (Huang et al., 2023a).

## 1 Introduction

Global terrestrial evapotranspiration (ET) is a vital component of the Earth's water cycle and energy budget. It includes evaporation from the soil and water surfaces (some studies also consider evaporation from the intercepted precipitation in canopies) and plant transpiration ~~(Zhang et al., 2021; He et al., 2022).~~(Zhang et al., 2021; He et al., 2022; Wang et al., 2021a). Accurate and timely estimation of ET is essential for quantitatively assessing changes in the water cycle under climate change, vigilant monitoring drought, and effectively managing and allocating water resources (Su et al., 2020; Han et al., 2021; Aschonitis et al., 2022).

~~While near~~Near-real-time ET estimation from climate models ~~is~~have been widely used to assess and predict ET changes in the global water cycle under different weather conditions (Copernicus Climate Change Service, 2020), While these models ~~often have limited~~such as ERA5 reanalysis offer near-real-time latent heat flux (ET in energy units) with a delay of just six days, they typically feature coarser spatial resolutions, ~~making them less effective~~often 0.1° or more. This level of resolution may limit their effectiveness for ~~assessing~~detailed assessments of drought conditions and ~~optimizing~~the optimization of water resource allocation. On the other hand, obtaining highly accurate, near-real-time, or real-time ET measurements through local eddy covariance or lysimeter methods can be very valuable (Awada et al., 2022), but collecting large-scale ET data using this equipment proves to be quite challenging ~~(Barrios et al., 2015; Tang et al., 2009)~~(Barrios et al., 2015; Tang et al., 2009).

~~Remote sensing presents a promising method for near-real-time estimation of global terrestrial ET by offering timely observed land surface data. Several satellite-based ET datasets have emerged in recent decades, each utilizing different algorithms such as the Penman-Monteith-based ET products like MODIS ET (MOD16), developed by Mu et al. (2007, 2011), the Advanced Very High Resolution Radiometer (AVHRR) ET by Zhang et al. (2006, 2009), and the Penman-Monteith-Leuning Evapotranspiration V2 (PML_V2, or simply PML) developed by Zhang et al. (2019, 2022). In addition, the Global Bio-Atmosphere Flux (GBAF, also known as FluxCom) uses a machine learning approach with data from flux towers, meteorology, and hydrology, published by Jung et al. (2009, 2010, 2019). Finally, the Priestley-Taylor equation-based Global Land Evaporation Amsterdam Model (GLEAM) ET was~~

~~developed by Miralles et al. (2011b) and Martens et al. (2017). While these satellite-based global ET products yield reasonable estimations, they cannot provide near-real-time ET estimates. Despite the ongoing rapid updates of the MOD16 ET dataset, it still encounters a delay~~Satellite remote sensing-based ET estimates outperform climate model simulations by offering high spatial resolution for detailed water use analysis, near-real-time data for prompt environmental response, and global coverage for comprehensive water cycle studies. These estimates rely on direct observations, enhancing accuracy, especially where ground data are sparse, and allow for the dynamic monitoring of land and vegetation changes. This capability underscores their importance in water resource management and climate research, complementing the broader perspectives provided by climate models.

The selected ET products discussed in this study embody diverse and innovative algorithmic approaches that have significantly contributed to global ET estimation and gained recognition within the scientific community. The MOD16 ET dataset, developed by Mu et al. (2007, 2011), utilizes a Penman-Monteith-based approach and is driven by MODIS land cover, albedo, fractional photosynthetically active radiation, leaf area index, and daily meteorological reanalysis data from NASA's Global Modelling and Assimilation Office to estimate ET. As the first satellite-based global ET product, it played a pivotal role in providing precise estimations crucial for global drought monitoring (Mu et al., 2013).

The AVHRR ET dataset, developed by Zhang et al. (2006, 2009), employed a modified Penman–Monteith approach over land, integrating biome-specific canopy conductance determined by NDVI, and utilized a Priestley–Taylor approach over water surfaces. These algorithms were driven by AVHRR Global Inventory Modeling and Mapping Studies (GIMMS) NDVI, daily surface meteorology data from the National Centers for Environment Prediction/National Center for Atmospheric Research (NCEP/NCAR) reanalysis, and solar radiation from NASA/GEWEX Surface Radiation Budget Release-3.0. This dataset has significantly advanced the study of the global water cycle, capitalizing on its extensive coverage and high accuracy to provide valuable insights into global hydrological processes.

The FLUXCOM dataset, is notable for its utilization of machine learning to integrate eddy covariance data from the global FLUXNET tower network, surface meteorological data, and remote sensing data. This approach has made a substantial contribution to resolving the evapotranspiration paradox and has cemented its status as a crucial tool widely acknowledged within the scientific community for elucidating intricate ET dynamics. (Jung et al., 2009, 2010, 2019).

Additionally, GLEAM, developed by Miralles et al. (2011b) and Martens et al. (2017), holds a prominent position as one of the best satellite-based ET products, known for its unparalleled accuracy and unique algorithmic approaches that have considerably advanced global ET estimation and enhanced our understanding of land surface evapotranspiration processes. Lastly, PML, developed by Zhang et al. (2019, 2022), represents the first 250-meter global coverage ET product, providing unprecedented spatial resolution for global ET estimation and contributing to our understanding of the decline in global water availability (Zhang et al., 2023b).

While these satellite-based global ET products provide reasonable estimations, they do not offer near-real-time ET estimates. Despite ongoing rapid updates to the MOD16 ET dataset, it still encounters delays exceeding two weeks. Additionally, AVHRR ET spans from 1983 to 2006, PML ET covers the period from 2002 to 2019, ~~GBAF~~FLUXCOM data covers from ~~2001~~1950 to ~~2015~~2016, and GLEAM ET extends from ~~2003~~2001 to ~~2020~~2022. Notably, the four later ET products exhibit data gaps exceeding one year, posing challenges for near-real-time estimation. ~~Additionally~~Furthermore, NASA's ECOsystem Spaceborne Thermal Radiometer Experiment on Space Station (ECOSTRESS) ~~intends~~aims to deliver global-scale ET estimation (Fisher et al., 2020). ~~Unfortunately~~However, as of now, the data from ECOSTRESS have not been published~~. This data gap means there is still~~, resulting in a lack of satellite-based global near-real-time ET estimation.

The Variation of the Moderate Resolution Imaging Spectroradiometer Standard Evapotranspiration Algorithm (VISEA) was introduced by Tang et al. (2009), which was designed for the near-real-time monitoring of crop consumption at the basin scale. Huang et al. (2017) examined its reliability by conducting a comprehensive assessment comparing its ET values with flux tower measurements and other gridded ET datasets across various scales in China. Subsequently, to improve the model, a decoupling parameter for daily evaporation fraction (EF) was introduced (Huang et al., 2021), and the atmospheric emissivity and cloud coverage in the daily net radiation calculation was included ~~(Huang et al., 2023b)~~(Huang et al., 2023b). Global terrestrial application and evaluation of the developed VISEA algorithm have not been conducted so far. In this study, we employ this VISEA algorithm along with MODIS surface reflectance (MOD09CMG) (Vermote, 2015), land surface temperature/emissivity (MOD11C1) (Wan et al., 2015), land cover products (MCD12C1) (Friedl & Sulla-Menashe, 2015), vegetation indices (MOD13C1) (Didan, 2015), albedo (MCD43C3) (Schaaf & Wang 2015), and hourly shortwave radiation from ECMWF ERA5-Land (Sabater, 2019) to provide global daily ET estimates from 2001 to 2022.

The performance of VISEA was evaluated with data from meteorological instruments and eddy covariance measurements at 149 flux towers of FLUXNET (Pastorello et al., 2020). We assessed the spatial distribution averages of VISEA by comparing its multi-year average with established ET datasets GLEAM (Martens et al., 2017; Miralles et al., 2011), ~~GBAF~~FLUXCOM (Jung et al., 2009, 2010, 2018), AVHRR (Zhang et al., 2009, 2010), MOD16 (Mu et al., 2007, 2011), PML (Zhang et al., 2019, 2022) and precipitation data from the Global Precipitation Climatology Centre (GPCC) (Udo et al., 2011).

## 2. Methods

### 2.1 Description of the VISEA algorithm

VISEA, short for the Variation of the Moderate Resolution Imaging Spectroradiometer Standard Evapotranspiration Algorithm, is a modification of the MODIS standard Evapotranspiration (ET) algorithm. The original MODIS algorithm, created by Mu et al. (2007 and 2011), is based on the Penman-Monteith method. VISEA introduces two significant modifications. First, it employs the Vegetation (VI)-Temperature (Ts) Triangle method, originally developed by Nishida et al. (2003), to estimate air temperature. Second, VISEA incorporates hourly data on shortwave downward radiation from the ERA5-Land dataset to calculate daily average energy. These two advancements enable VISEA to estimate large-scale ET without needing local measurements as supplementary data.

Unlike energy budget-based ET algorithms (such as SEBS, METRIC, and Alexi~~) that rely on)~~, which calculate ET (latent heat flux) as the ~~direct use~~residual of ~~thermal information,~~the net radiation, subtracting soil heat flux and sensible heat flux. VISEA estimates ET using the Penman-Monteith equation, placing it in a different category of satellite-based global ET products currently in use. VISEA is a two-source model, which means the $ET$ in one grid cell was separated as the transpiration from full vegetation cover and the evaporation from bare soil surface if energy transfer from the vegetation to the soil surface was ignored (Nishida et al., 2003), i.e.,

$$ET = f_{veg}ET_{veg} + (1 - f_{veg})ET_{soil} \tag{1}$$

~~where the subscript "$veg$" means full vegetation cover and the subscript "soil" indicates the soil exposed to solar radiation (called bare soil); $ET_{veg}$ is the transpiration from full vegetation cover area (W m$^{-2}$), $ET_{soil}$ is the evaporation from bare soil (W m$^{-2}$), $f_{veg}$ is the portion of the area with the vegetation cover, which can be calculated by Normalized Difference Vegetation Index, NDVI (Tang et al., 2009):~~

where the subscript "$veg$" means full vegetation cover and the subscript "soil" indicates the soil exposed to solar radiation (called bare soil); $ET_{veg}$ is the transpiration from full vegetation cover area (W m$^{-2}$), $ET_{soil}$ is the evaporation from bare soil (W m$^{-2}$), $f_{veg}$ is the portion of the area with the vegetation cover, which can be calculated by Normalized Difference Vegetation Index (calculation details are provided in Appendix A, Tang et al., 2009)

$$\cancel{f_{veg} = \frac{NDVI - NDVI_{min}}{NDVI_{max} - NDVI_{min}}} \tag{2}$$

~~where the $NDVI$ is the Normalized Difference Vegetation Index and can be calculated as:~~

$$\cancel{NDVI = \frac{R_{nir} - R_{red}}{R_{nir} + R_{red}}} \tag{3}$$

~~where $NDVI_{min}$ is the $NDVI$ of the bare soil without plants and $NDVI_{max}$ is the $NDVI$ of the full vegetation cover, $R_{nir}$ is the near-infrared reflectance and $R_{red}$ is the red reflectance. The daily reflectance $R_{nir}$ and $R_{red}$ were measured by MODIS reflectance data MOD09CMG (Fig. 1). Based on Tang et al. (2009), we set $NDVI_{min}$ = 0.22 and $NDVI_{max}$ = 0.83. Missing observation for the daily MOD09CMG calculated $NDVI$ data was filled with the 16-day averaged $NDVI$ values in the MOD13Q1data product (Fig. 1).~~

The available energy $Q$ (W m$^{-2}$), which is the sum of the latent heat flux and sensible heat flux (also known as the net radiation minus soil heat flux) is also separated into the available energy for vegetation transpiration, $Q_{veg}$ (W m$^{-2}$) and $Q_{soil}$ (W m$^{-2}$) for bare soil evaporation, which was expressed by Nishida et al. (2003) as:

$$Q = f_{veg}Q_{veg} + (1 - f_{veg})Q_{soil} \tag{4}$$

**带格式的:** 缩进: 首行缩进: 0.74 厘米

As satellites like Terra and Aqua provide instantaneous snapshot observations of the Earth only once a day, a temporal scaling method is needed to convert instantaneous measurements into daily ET values. Nishida et al. (2003) used satellite-based noon time instantaneous evaporation fraction ($EF$), defined as the ratio of latent heat flux ($ET$) to available energy as daily $EF$ ($EF = \frac{ET}{Q}$ ~~)~~), the calculation of instantaneous $EF$ is described at Appendix B), multiplied the daily $Q$ to calculated daily $ET$ based on the assumption that $EF$ is constant over a day:

$$ET = EF\ Q \tag{5}$$

In the next section, we will detail how VISEA calculates the daily $EF$, and Q in Equation (5), and also daily air and Ts, land surface ~~temperatures~~temperature.

### 2.1.1 Daily evaporation fraction calculation

~~Combining Eq. 1 and 4, we fist calculated the instantaneous evaporation fraction, $EF^i$ as:~~

$$\cancel{EF^i = f_{veg}\frac{Q^i_{veg}}{Q^i}EF^i_{veg} + (1 - f_{veg})\frac{Q^i_{soil}}{Q^i}EF^i_{soil}} \tag{6}$$

~~where the superscript $i$ stands for the instantaneous value of the parameter, $EF^i_{veg}$ and $EF^i_{soil}$ are the instantaneous full vegetation coverage and bare soil $EF$, respectively. $EF^i_{veg}$ can be expressed as a function of instantaneously parameters as ( Nishida et al., 2003):~~

$$\cancel{EF^i_{veg} = \frac{\alpha\,\Delta^i}{\Delta^i+\gamma(1+r^i_{c\,veg}/2r^i_{a\,veg})}} \tag{7}$$

~~where α is the Priestley-Taylor parameter, which was set to 1.26 for wet surfaces (De Bruin, 1983); $\Delta^i$ is the slope of the saturated vapor pressure, which is a function of the temperature (Pa K$^{-1}$); $\gamma$ is the psychometric constant (Pa K$^{-1}$); $r^i_{c\,veg}$ is the instantaneous surface resistance of the vegetation canopy (s m$^{-1}$); $r^i_{a\,veg}$ is the instantaneous aerodynamics resistance of the vegetation canopy (s m$^{-1}$). $EF^i_{soil}$ was expressed by Nishida et al. (2003) as a function of the instantaneous soil temperature and the available energy based on the energy budget of the bare soil:~~

$$\cancel{EF^i_{soil} = \frac{T^i_{soil\,max}-T^i_{soil}}{T^i_{soil\,max}-T^i_{a}}\frac{Q^i_{soil0}}{Q^i_{soil}}} \tag{8}$$

~~where $T^i_{soil\,max}$ is the instantaneous maximum possible temperature at the surface reached when the land surface is dry (K), $T^i_{soil}$ is the instantaneous temperature of the bare soil (K), $T^i_{a}$ is the instantaneous air temperature, $Q^i_{soil0}$ is the instantaneous available energy when $T^i_{soil}$ is equal to $T^i_{a}$ (W m$^{-2}$).~~

As the assumption of $EF^i = EF^d$ caused 10%-30% underestimation of daily ET (Huang et al., 2017; Yang et al., 2013), we introduced a decoupling parameter to covert $EF^i$ into $EF^d$ following the algorithm of Tang et al. (2017a, 2017b). This new decoupling parameter-based evaporation faction is developed from Penman-Monteith and McNaughton-Jarvis mathematical equations:

$$EF^d = EF^i\frac{\Delta^d}{\Delta^d+\gamma}\frac{\Delta^i+\gamma}{\Delta^i}\frac{\Omega^{*i}}{\Omega^{*d}}\frac{\Omega^d}{\Omega^i} \qquad (9~~6~~)$$



**带格式的:** 缩进: 首行缩进: 0.74 厘米

**带格式的:** 段落间距段后: 1 行

where superscript "$d$" means daily; the $EF^i$ is the instantaneous evaporation fraction; Ω is the decoupling factor that represents the relative contribution of radiative and aerodynamic terms to the overall evapotranspiration (Tang and Li, 2017), $\Omega_i^*$ is the value of the decoupling factor, Ω, for wet surfaces. According to Pereira (2004), Ω and $\Omega^*$ ~~can be expressed as:~~(the calculation details is presented in Appendix C).

$$\cancel{\Omega = \frac{1}{1+\frac{\gamma}{\Delta+\gamma}\frac{r_c}{r_a}}} \qquad \cancel{(10)}$$

$$\cancel{\Omega^* = \frac{1}{1+\frac{\gamma}{\Delta+\gamma}\frac{r^*}{r_a}}} \qquad \cancel{(11)}$$

$$\cancel{r^* = \frac{(\Delta+\gamma)\rho C_p VPD}{\Delta\gamma(R_n-G)}} \qquad \cancel{(12)}$$

~~where $r_c$ is the surface resistance (s m$^{-1}$); $r_a$ is the aerodynamic resistance (s m$^{-1}$); the calculation details of instantaneous and daily $r_c$ and $r_a$ for vegetation and soil are explained in Appendix A. $r^*$ is the critical surface resistance when the actual evapotranspiration equals the potential evaporation (called equilibrium evapotranspiration, s m$^{-1}$); $\rho$ is the air density (kg m$^{-3}$); $C_p$ is the specific heat of the air (J kg$^{-1}$ K$^{-1}$); $VPD$ is the vapor pressure deficit of the air (Pa). Δ is the slope of the saturated vapor pressure (Pa K$^{-1}$).~~

For full vegetation-covered areas, $EF_{veg}^d$ is expressed as:

$$EF_{veg}^d = \frac{\alpha\,\Delta^i}{\Delta^i+\gamma\left(1+\frac{r_{c\,veg}^i}{2r_{a\,veg}^i}\right)}\left(\frac{\Delta^d}{\Delta^d+\gamma}\frac{\Delta^i+\gamma}{\Delta^i}\frac{\Omega_{veg}^{*\,i}}{\Omega_{veg}^{*\,d}}\frac{\Omega_{veg}^d}{\Omega_{veg}^i}\right) \tag{\cancel{13}7}$$

$r_{c\,veg}^i$ is the instantaneous canopy resistance (s m$^{-1}$), $r_{a\,veg}^i$ is the instantaneous aerodynamic resistance (s m$^{-1}$). Determining these resistances are presented in Appendix D.

For bare soil, $EF_{soil}^d$ is calculated as:

$$EF_{soil}^d = \frac{T_{soil\,max}^i - T_{soil}^i}{T_{soil\,max}^i - T_a^i}\,\frac{Q_{soil\,0}^i}{Q_{soil}^i}\left(\frac{\Delta^d}{\Delta^d+\gamma}\frac{\Delta^i+\gamma}{\Delta^i}\frac{\Omega_{soil}^{*\,i}}{\Omega_{soil}^{*\,d}}\frac{\Omega_{soil}^d}{\Omega_{soil}^i}\right) \tag{\cancel{14}8}$$

Thus, $EF^d$ is expressed as:

$$EF^d = f_{veg}\frac{Q_{veg}^i}{Q^i}\,EF_{veg}^d + (1-f_{veg})\frac{Q_{soil}^i}{Q^i}\,EF_{soil}^d \tag{\cancel{15}9}$$

### 2.1.2 Daily calculation of available energy $Q_{veg}^d$ and $Q_{soil}^d$

~~The daily available energy $Q$ (W m$^{-2}$) for the vegetation and the bare soil surface is calculated by the energy balance equation:~~

We used an improved daily available energy $Q$ (W m$^{-2}$) method (Huang et al., 2023) for the vegetation and the bare soil surface is calculated by the energy balance equation:

$$R_n - G = Q$$ (~~16~~10)

~~where $R_n$ is the net radiation (W m^-2^), which could be calculated by the land surface energy balance; $G$ is the soil heat flux (W m^-2^). ( $G$≈0 on a daily basis),~~

$$\cancel{R_n^d = (1 - albedo^d)R_d^d - \varepsilon_s^d \sigma T_s^{d\,4} + (1 + Cloud^d)\varepsilon_a^d \sigma\, T_a^{d\,4}}$$ ~~(17)~~

~~where $albedo^d$ is the daily albedo of the soil surface; $R_d^d$ is daily incoming shortwave radiation (W m^-2^); $\varepsilon_s^d$ and $\varepsilon_a^d$ are the daily emissivity of land surface and atmosphere (Brutsaert, 1975; Wang and Dickinson, 2013; details are presented in Appendix B ), $\varepsilon_s^d$ can be retried by MOD11C1; $\sigma$ is the Stefan-Boltzmann constant; $T_a^d$ is the daily near surface air temperature (K); $T_s^d$ is the daily surface temperature (K).~~

~~For the downward longwave radiation, we~~where $R_n$ is the net radiation (W m$^{-2}$), which could be calculated by the land surface energy balance; $G$ is the soil heat flux (W m$^{-2}$), $G$≈0 on a daily basis (Fritschen and Gay, 1979; Nishida et al., 2003; Tang et al., 2009),

$$R_n^d = (1 - albedo^d)R_d^d - \varepsilon_s^d \sigma T_s^{d\,4} + (1 + Cloud^d)\varepsilon_a^d \sigma\, T_a^{d\,4}$$ (11)

Where $albedo^d$ is the daily albedo of the soil surface; $R_d^d$ is daily incoming shortwave radiation (W m$^{-2}$), obtained the ERA5_Land shortwave radiation (we called ERA5_Rd); $\varepsilon_s^d$ and $\varepsilon_a^d$ are the daily emissivity of land surface and atmosphere; different from the former study provided by Huang et al., (2021), which set we $\varepsilon_s^d$ and $\varepsilon_a^d$ equal, we calculated the $\varepsilon_a^d$ by Appendix E flowing study of Brutsaert, (1975) and Wang and Dickinson(2013), $\varepsilon_s^d$ can be retried by MOD11C1; $\sigma$ is the Stefan-Boltzmann constant; $T_a^d$ is the daily near surface air temperature (K); $T_s^d$ is the daily surface temperature (K).

We account for the influence of clouds by assuming a linear correlation between downward longwave radiation and cloud coverage~~:~~ in the calculation of downwards longwave radiation based on the study of Huang et al., (2023):

$$Cloud = (1 - K_t)$$ (~~18~~12)

$$K_t = \frac{R_d^d}{R_a^d}$$ (~~19~~13)

$Cloud^d$ is derived from the clearness index $K_t$ (Chang and Zhang, 2019; Goforth et al., 2002). $R_a^d$ is the daily extraterrestrial radiation calculated by the FAO (1998).

According to Huang et al. (~~2021~~2023), $Q_{veg}^d$ can be calculated by assuming as $T_s^d = T_a^d$ according to the VI-Ts method which implies that the minimum land surface temperature occurs in fully vegetated grid cells and is equivalent to $T_a^d$.

$$Q_{veg}^d = (1 - albedo^d)R_d^d + (1 + Cloud^d)\varepsilon_a^d \sigma\, T_a^{d\,4} - \varepsilon_s^d \sigma T_s^{d\,4}$$ (~~20~~14)

$$Q_{soil}^d = (1 - C_G)(1 - albedo^d)R_d^d + (1 + Cloud^d)\varepsilon_a^d \sigma\, T_a^{d\,4} - \varepsilon_s^d \sigma T_s^{d\,4}$$ (~~21~~15)

域代码已更改

Thus, $(1+Cloud^d)\varepsilon_a^d\sigma\, {T_a^d}^4$ is the daily downward longwave radiation (W m$^{-2}$), and $\varepsilon_s^d\sigma {T_s^d}^4$ is the daily upward longwave radiation (W m$^{-2}$), where $C_G$ is an empirical coefficient ranging from 0.3 for a wet soil to 0.5 for a dry soil (Idso et al., 1975).

Following the study of Huang et al. (~~2021~~2023), the daily $ET^d$ can be calculated by the daily $EF^d$ and $Q^d$ as:

$$ET^d = EF^d Q^d \qquad (\cancel{22}16)$$

Figure 1 illustrates the workflow of VISEA.



**带格式的:** 段落间距段后: 1 行

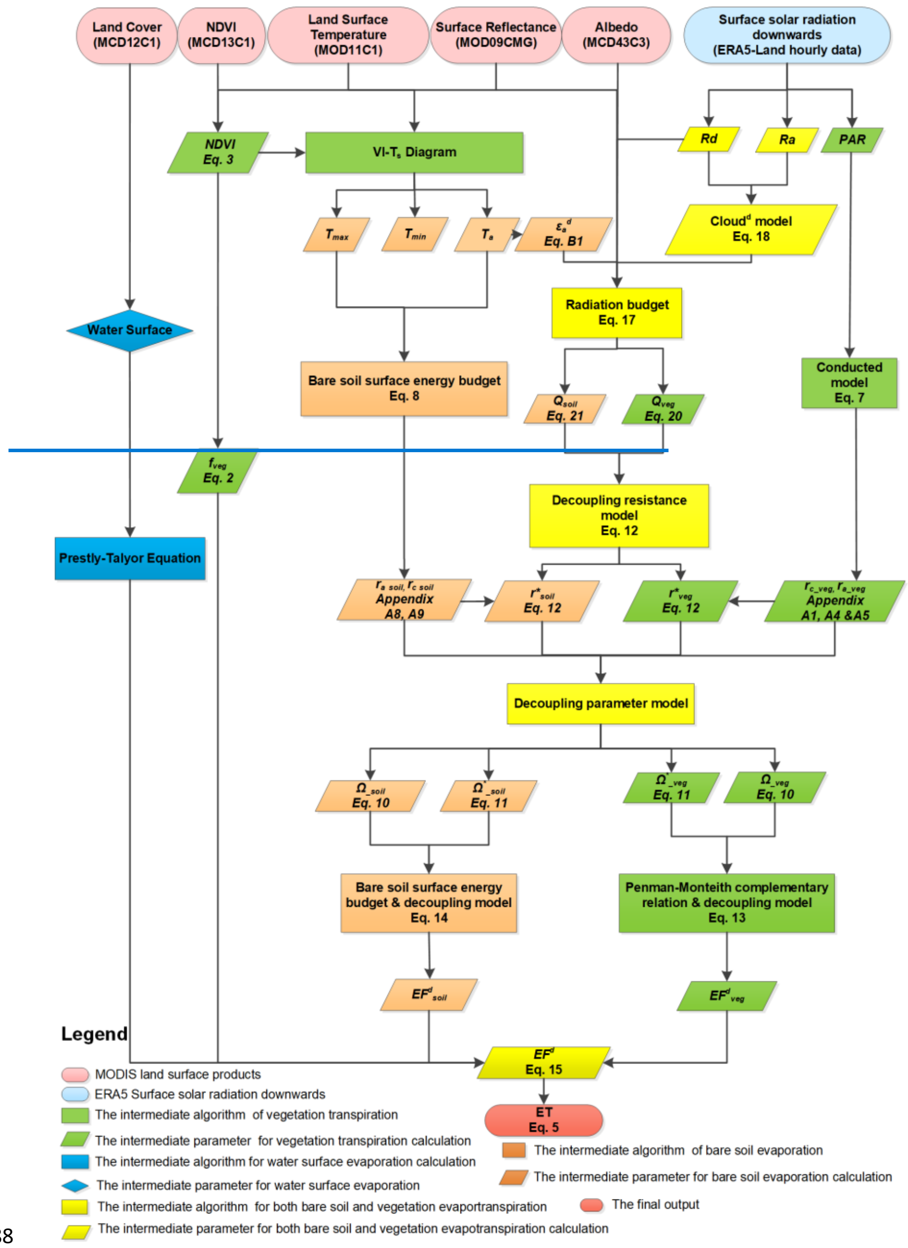

Land Cover (MCD12C1)
NDVI (MCD13C1)
Land Surface Temperature (MOD11C1)
Surface Reflectance (MOD09CMG)
Albedo (MCD43C3)
Surface solar radiation downwards (ERA5-Land hourly data)
NDVI Eq. 3
VI-Ts Diagram
Rd
Ra
PAR
Tmax
Tmin
Ta
εa d Eq. B1
Cloud d model Eq. 18
Water Surface
Radiation budget Eq. 17
Bare soil surface energy budget Eq. 8
Qsoil Eq. 21
Qveg Eq. 20
Conducted model Eq. 7
fveg Eq. 2
Decoupling resistance model Eq. 12
Prestly-Talyor Equation
ra soil, rc soil Appendix A8, A9
r*soil Eq. 12
r*veg Eq. 12
rc_veg, ra_veg Appendix A1, A4 &A5
Decoupling parameter model
Ω_soil Eq. 10
Ω'_soil Eq. 11
Ω'_veg Eq. 11
Ω_veg Eq. 10
Bare soil surface energy budget & decoupling model Eq. 14
Penman-Monteith complementary relation & decoupling model Eq. 13
EF d soil
EF d veg
Legend
EF d Eq. 15
ET Eq. 5
MODIS land surface products
ERA5 Surface solar radiation downwards
The intermediate algorithm of vegetation transpiration
The intermediate parameter for vegetation transpiration calculation
The intermediate algorithm for water surface evaporation calculation
The intermediate parameter for water surface evaporation
The intermediate algorithm for both bare soil and vegetation evapotranspiration
The intermediate parameter for both bare soil and vegetation evapotranspiration calculation
The intermediate algorithm of bare soil evaporation
The intermediate parameter for bare soil evaporation calculation
The final output

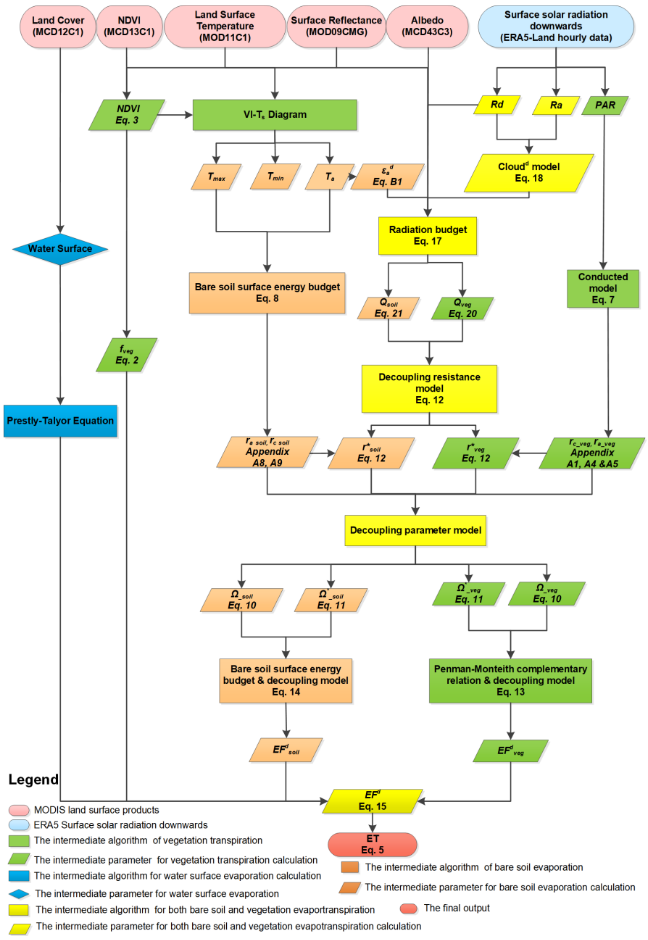


**Figure 1.** Schematic of VISEA algorithm. The ovals in the top row are the databases, and the square boxes are the algorithms, and parallelograms are the parameters. The numbers in the parenthesis are the equation to determine the parameters.

### 2.1.3 The calculation of daily air temperature, $T_a^d$ and surface temperature, $T_{\cancel{a}s}^d$

Daily air temperature, $T_a^d$ ~~Is~~is a critical parameter in the VISEA algorithm, used in calculations for downward longwave radiation, daily aerodynamic resistance, and surface resistance. The key innovation in calculating $T_a^d$, involves employing the VI-Ts method to estimate instantaneous air temperature, $T_a^i$ during the daytime.

This method was developed based on the empirical linear relationship between surface temperature (Ts) and Vegetation Index (VI). Surface temperature increases when the vegetation index decreases, and conversely, surface temperature decreases when the vegetation index increases. By defining a "window" formed by the neighboring 5 * 5 grid cells, the scatter plot of these 25 grid cells' VI and Ts typically exhibits a triangular (or trapezoidal) distribution. In this scatter plot, we identify the "warm edge" (characterized by a low vegetation cover fraction and high Ts) and the "cold edge" (marked by a high vegetation cover fraction and low Ts).

Through simple interpolation, Ts corresponding to any given vegetation condition within the range of the "warm edge" and "cold edge" can be determined. The lowest Ts could be determined by the highest VI, and the highest Ts could be determined by the lowest VI. Therefore, following Nishida et al. (2003), under the assumption that the lowest surface temperature equals the air temperature (Ta), we can derive the daily air temperature.

For nighttime periods, it is assumed that air temperature is equivalent to the nighttime land surface temperature provided by MOD11C1. These two temperature estimates are then extended into hourly air temperature profiles using a sine-cosine fitting curve. The 24-hour average of $T_a^i$ is used as $T_a^d$. Similarly, $T_s^d$ is calculated using MOD11C1 land surface temperature data for both daytime and nighttime. These estimates are extended into hourly surface temperature profiles using a similar sine-cosine fitting curve, and the daily average of $T_s^d$ is determined (Huang et al., 2021).

带格式的: 缩进: 首行缩进: 0.74 厘米, 孤行控制

A key advance of this VISEA algorithm is the application of the VI-Ts method to calculate $T_{soil\ max}^i$ and $T_a^i$ (Huang et al., 2017; Nishida et al., 2003; Tang et al., 2009). The VI-Ts method is based on the empirical linear relationship between the vegetation index (VI), typically calculated by NDVI, and land surface temperature (Ts). When plotted on a two-dimensional scatter plot, VI and Ts generally form a trapezoid or triangular shape. In these plots, regions with low VI and high Ts values constitute the "warm edge," while areas with high VI and low Ts values form the "cold edge." Using simple linear interpolation, Ts values corresponding to any given VI between the "warm edge" and the "cold edge" can be determined. Assuming$T_s = T_a^i$ for cases where the highest VI corresponds to the lowest Ts, we can calculate $T_a^i$. Similarly, $T_{soil\ max}^i$ can be easily calculated since it corresponds to the lowest VI.

This VI-Ts method allows for the estimation of $T_a^i$ and $T_{soil\ max}^i$ without the need for additional meteorological data. However, ~~it's worth noting that~~ some studies have found that the VI-Ts method may not consistently provide satisfactory results, especially in colder regions where vegetation thrives better under higher temperatures.

### 2.2 Technical validation

The correlation coefficient, Root Mean Square Error (RMSE) and Nash-Sutcliffe efficiency coefficient are used to evaluate our global daily ET estimates with eddy covariance measurements and compared with the other five independent global ET products on a monthly scale.

The correlation coefficient R is calculated as:

$$R = \frac{\sum(X-\bar{X})(Y-\bar{Y})}{\sqrt{\sum(X-\bar{X})^2\sum(Y-\bar{Y})^2}} \qquad (\cancel{23}17)$$

$R$ is the correlation coefficient; $X$ is the estimated variable; $\bar{X}$ is the average of $X$; Y is the observed variable; $\bar{Y}$ is the average of $Y$.

The Root Mean Square Error (RMSE) is calculated as:

$$RMSE = \sqrt{\frac{\sum_{i=1}^{N}(X_i - Y_i)^2}{N}}$$ (~~24~~18)

For a more nuanced understanding of the Root Mean Square Error (RMSE), we have deconstructed it into two distinct components: RMSEs (systematic RMSE) and RMSEu (unsystematic RMSE). This breakdown allows a more detailed examination of the systematic and unsystematic sources contributing to the overall error metric.

The systematic Root Mean Square Error (RMSEs) is calculated as:

$$RMSEs = \sqrt{\frac{\sum_{i=1}^{N}(Z_i - Y_i)^2}{N}}$$ (~~25~~19)

The unsystematic Root Mean Square Error (RMSEu) is calculated as:

$$RMSEu = \sqrt{\frac{\sum_{i=1}^{N}(Z_i - X_i)^2}{N}}$$ (~~26~~20)

Where $Z_i = a + bY_i$, where a and b are the least squares regression coefficients of the estimated variable $X_i$ and observed variable $Y_i$, $N$ is the sample size (Norman et al., 1995).

The Nash-Sutcliffe efficiency coefficient (NSE)

$$NSE = 1 - \frac{\sum(X_i - Y_i)^2}{\sum(Y_i - \bar{Y})^2}$$ (~~27~~21)

The ratio of the standard deviations of $X$ and $Y$

$$Ratio = \frac{X_{Standard\ Deviation}}{Y_{Standard\ Deviation}}$$ (~~28~~22)

The Bias of $X$ and $Y$

$$Bias = \bar{X} - \bar{Y}$$ (~~29~~23)

**2.3 The gap-filling of MODIS data**

MODIS sensors on board of Terra and Aqua observe the Earth twice a day. However, there are always data gaps in the MODIS land products because of cloud cover problems. In the VISEA algorithm, we used the neighboring days' available data to fill the data gaps. According to the study of Tang et al. (2009), the cloud gaps don't reduce the accuracy of this algorithm significantly.

## 3. Data

### 3.1 The input data

The input data including the MODIS land products: daily 0.05° surface reflectance (MOD09CMG), land surface temperature/emissivity (MOD11C1) and albedo (MCD43C3), 8-day 0.05° vegetation indices (MOD13C1) and yearly 0.05° land cover products (MCD12C1). We also used hourly downward surface solar radiation from the Fifth Generation of the European Centre for Medium-Range Weather Forecasts (ECMWF) Reanalysis (ERA5), "ERA5-Land hourly data from 1950 to present" data as energy input of VISEA algorithm. The surface solar radiation data from ERA5-Land and land data products from MODIS land products are both near-real-time datasets with a one-week delay, enabling VISEA to provide global near-real-time ET estimations. Details of the input data, their download links, variable names, used parameters, spatial and temporal resolution are given in Table 1.

**Table 1. The input of VISEA**

| **The input of VISEA** | | | |
|---|---|---|---|
| **Data source** | Data name | Used parameter | Spatial/temporal resolution |
| **MODIS Land Product** | MOD11C1 | Land Surface Temperature | 0.05°/ daily |
| | MOD09CMG | Surface Reflectance | 0.05°/daily |
| | MCD43C3 | Albedo | 0.05°/daily |
| | MOD13C1 | NDVI | 0.05°/16-day |
| | MCD12C1 | Land cover | 0.05°/ yearly |
| **ERA5-Land hourly data** | Rd | Downward surface solar radiation | 0.1°/ hourly |

### 3.2 The evaluation data

#### 3.2.1 The flux tower measurements from FLUXNET

We evaluated the accuracy of ~~daily averaged~~the input ERA5-Land shortwave radiation, ~~VISEA~~ estimated daily net radiation, air temperature, and ET by comparing them ~~with~~against measurements from FLUXNET2015 ~~flux towers FLUXNET2015: CC-BY-4.0~~ (Pastorello et al., 2020) ~~(https://fluxnet.org/data/download-data/). we compared its results with measurements obtained from FLUXNET2015: CC-BY-4.0 15, which can be accessed at https://fluxnet.org/data/download-data/. While there are records from a total of 212 flux towers in our datasets, not all of them met our stringent inclusion criteria. Each site needed to fulfill three specific requirements to be included in our analysis: (1) availability of data for the period spanning from 2001 to 2015; (2) ERA5-Land downward shortwave radiation greater than 0 within the 0.1° × 0.1° grid cell corresponding to the flux tower's location; (3) conformity with MODIS land cover data (MCD12C1) at the 0.05° × 0.05° grid cell level, ensuring that the flux tower was situated on land rather than over the ocean.~~

~~As a result, our~~. The data from FLUXNET2015 can be obtained at https://fluxnet.org/data/download-data. While there are records from a total of 212 flux towers in our datasets, not all of them met our stringent inclusion criteria. Each site needed to fulfil three specific requirements to be included in our analysis: (1) availability of data for the period spanning from 2001 to 2015; (2) ERA5-Land downward shortwave radiation greater than 0 within the 0.1° × 0.1° grid cell corresponding to the flux tower's location; (3) conformity with MODIS land cover data (MOD12C1) at the 0.05° × 0.05° grid cell level, ensuring that the flux tower was situated on land rather than over the ocean. In our evaluation using FLUXNET observational data, we leveraged FLUXNET's diligent efforts in addressing energy closure concerns. Specifically, FLUXNET has implemented rigorous measures for energy closure corrections and validations, thereby enhancing the reliability of the observational data from the 212 globally distributed flux towers (Pastorello et al., 2020; Baldocchi et al., 2001; Wang et al., 2022). We selected data spanning the period from 2001 to 2015 and excluded sites where ERA5-Land downward shortwave radiation was zero.

Our study incorporates data from a carefully selected subset of 149 flux towers that met these stringent criteria. This approach ensures the reliability and relevance of our analysis. The distribution of these 149 flux towers is presented in Figure 2. Supplementary Table S1 shows the longitude, latitude, elevation, and land cover type (classified by the International Geosphere-Biosphere Programme, IGBP) of these sites. The 149 sites covered 12 IGBP land cover types: 18 croplands (CRO), 1 closed shrublands (CSH), 15 deciduous broadleaf forests (DBF), 1 deciduous needle leaf forest (DNF), 10 evergreen broadleaf forests (EBF), 34 evergreen needle leaf forests (ENF), 30 grasslands (GRA), 5 mixed forests (MF), 8 open shrublands (OSH), 8 savannas (SAV), 13 wetlands (WET), and 6 woody savannas (WSA).

### 3.2.2 The other gridded ET and precipitation products

We also used five independent globally gridded ET and one precipitation products for VISEA estimated ET's comparison. The five ET products include two MODIS-based ET products: MOD16 (Mu et al., 2007, 2011) and Penman-Monteith-Leuning Evapotranspiration V2 (PML) (Zhang et al., 2019, 2022), one AVHRR-based AVHRR ET (Zhang et al., 2009, 2010), one machine learning algorithm output, the ~~Global Bio-Atmosphere Flux (GBAF)~~FLUXCOM ET data (Jung et al., 2009, 2010, 2018, 2019) and one multiple-satellites data based Global Land Evaporation Amsterdam Model (GLEAM) ET (Martens et al., 2017; Miralles et al., 2011). The precipitation data was from the Global Precipitation Climatology Centre (GPCC), which is based on local measurements (Schneider et al., 2014, 2017; Becker et al., 2013) and Global Unified Gauge-Based Analysis of Daily Precipitation (GPC). Details of these five ET products and the precipitation data are given in Table 2. To maintain the consistency in temporal and spatial resolution for comparison purposes, we obtained monthly MOD16 and PML, despite their original temporal resolution of 8 days and used the 0.05°×0.05° version of MOD16, AVHRR ET and PML. Additionally, for multi-year scale comparisons, we confined our dataset to the timeframe between 2001 and 2020. We also incorporated daily Evapotranspiration (ET) data from GLEAM and VISEA, alongside precipitation data from the Climate Prediction Center (CPC), spanning from July $25^{\text{th}}$ to August $2^{\text{nd}}$, 2022. This allowed for near-real-time analysis of ET and precipitation during the Yangtze River drought incident within that interval, despite the datasets potentially encompassing more extensive periods.

**Table 2.** The five global girded ET products and one precipitation product used for comparison with our

**带格式的:** 段落间距段后: 1 行, 无孤行控制

near-real-time global daily terrestrial ET estimates.

| Product name | Spatial/Temporal resolution | Time period | Theory |
|---|---|---|---|
| **GLEAM** | 0.25°/Monthly | ~~2002-2019~~2001-2022 | Priestly-Taylor Equation |
| **~~GBAF~~FLUXCOM** | 0.5°/Monthly | 2001-~~2008~~2016 | Machine learning |
| **MOD16** | 0.05°/~~8-day~~Monthly | 2001-~~2013~~2014 | Penman-Monteith Equation |
| **AVHRR** | 1°/Monthly | 2001-2006 | Improved Penman-Monteith Equation |
| **PML** | 0.05°/8-day | 2003-2018 | Penman-Monteith Equation and a diagnostic biophysical model |
| **GPCC** | 0.25°/Monthly | 2001-2019 | in-situ observations |
| **GPC** | 0.5°/Daily | 08/28/2022-09/01/2022 | Global Unified Gauge-Based Analysis of Daily Precipitation |

**设置了格式:** 字体: 8 磅

**设置了格式:** 字体: 8 磅

**设置了格式:** 字体: 8 磅

**设置了格式:** 字体: 8 磅

**设置了格式:** 字体: 8 磅

**设置了格式:** 字体: 8 磅

**设置了格式:** 字体: 8 磅

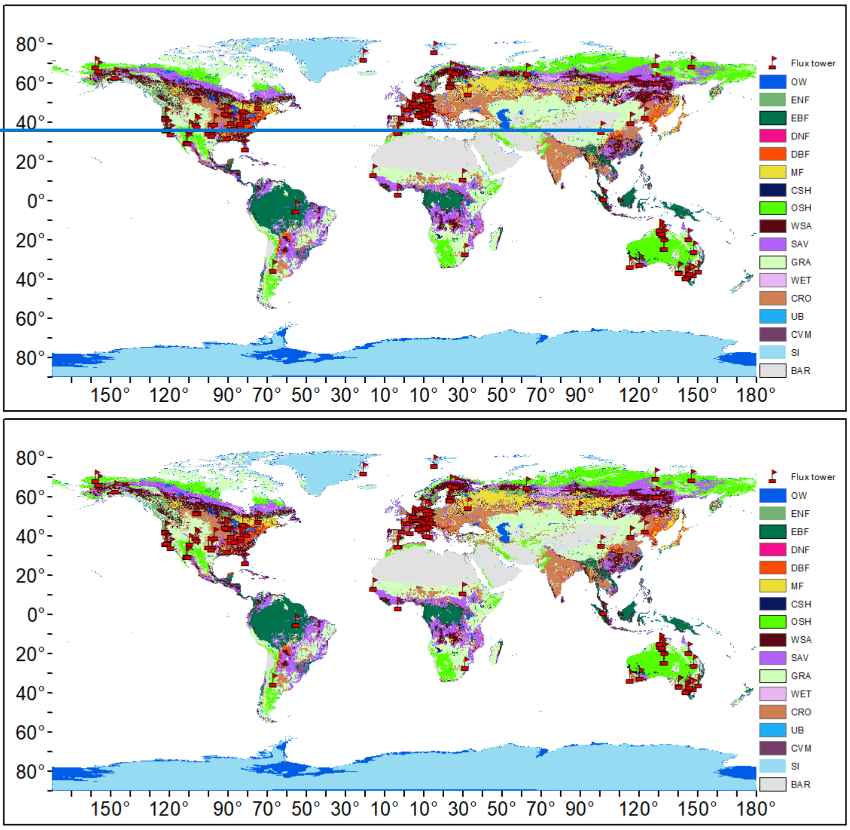


**Figure 2.** The distribution of 149 flux towers from FLUXNET in different IGBP land cover types, specifically OW (Water bodies), ENF (Evergreen needle leaf forests), EBF (Evergreen broadleaf forests), DNF (Deciduous needle leaf forests), DBF (Deciduous broadleaf forests), MF (Mixed forests), CSH (Closed shrublands), OSH (Open shrublands), WSA (Woody savannas), SAV (Savannas), GRA (Grasslands), WET (Permanent wetlands), CRO (Croplands), UB (Urban and built-up lands), CVM (Cropland/natural vegetation mosaics), SI (Snow and ice), BAR (Barren).

**设置了格式:** 字体: 非加粗

**带格式的:** 左, 行距: 单倍行距

## 4. Results

In our initial analysis, we juxtaposed downward solar radiation input data from ERA5-Land (ERA5_Rd) with measurements obtained from 149 flux towers (Obv_Rd) across diverse IGBP land cover types, as illustrated in Figure 3. The results indicate a commendable agreement between ERA5_Rd and Obv_Rd measurements for the majority of land covers, with notable exceptions observed in savanna (SAV). Specifically, the mean Nash-Sutcliffe Efficiency (NSE) stands at 0.84, the mean correlation coefficient (R) at 0.92, and the mean Root Mean Square Error (RMSE) at 38.3 W $m^{-2}$. This comparative analysis offers helpful insights into the performance of ERA5_Rd across different land cover categories.

447

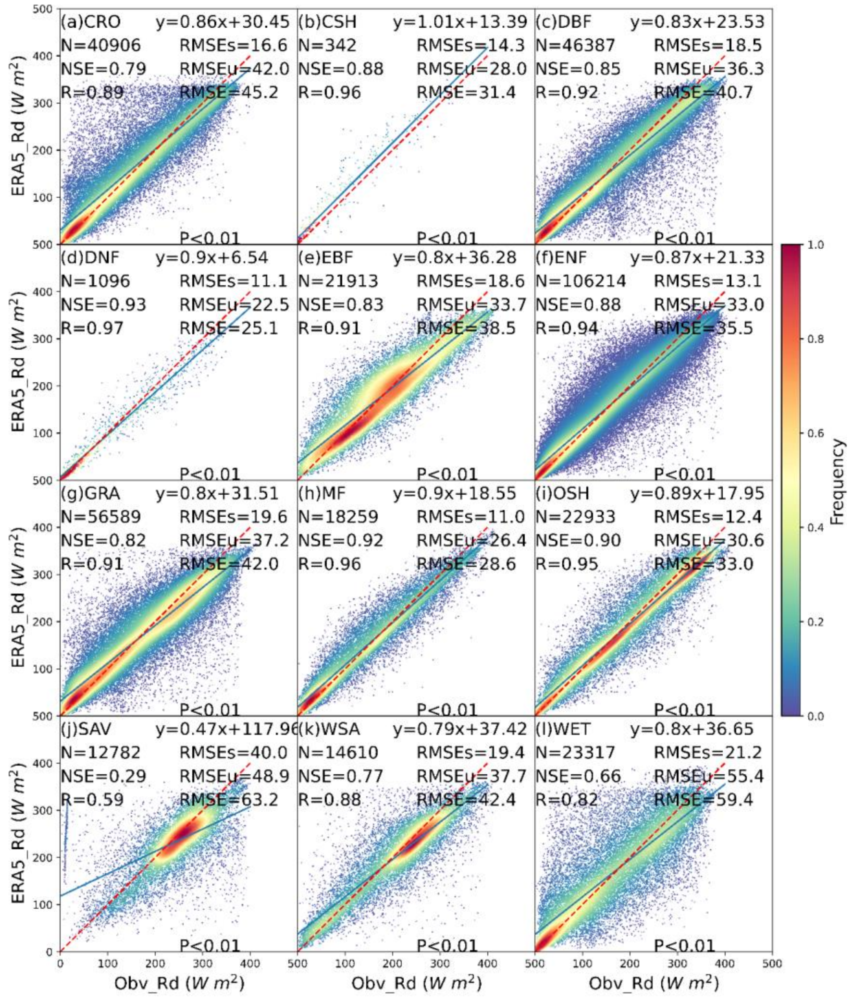

(a)CRO
y=0.86x+30.45
N=40906
RMSEs=16.6
NSE=0.79
RMSEu=42.0
R=0.89
RMSE=45.2
P<0.01
(b)CSH
y=1.01x+13.39
N=342
RMSEs=14.3
NSE=0.88
RMSEu=28.0
R=0.96
RMSE=31.4
P<0.01
(c)DBF
y=0.83x+23.53
N=46387
RMSEs=18.5
NSE=0.85
RMSEu=36.3
R=0.92
RMSE=40.7
P<0.01
(d)DNF
y=0.9x+6.54
N=1096
RMSEs=11.1
NSE=0.93
RMSEu=22.5
R=0.97
RMSE=25.1
P<0.01
(e)EBF
y=0.8x+36.28
N=21913
RMSEs=18.6
NSE=0.83
RMSEu=33.7
R=0.91
RMSE=38.5
P<0.01
(f)ENF
y=0.87x+21.33
N=106214
RMSEs=13.1
NSE=0.88
RMSEu=33.0
R=0.94
RMSE=35.5
P<0.01
(g)GRA
y=0.8x+31.51
N=56589
RMSEs=19.6
NSE=0.82
RMSEu=37.2
R=0.91
RMSE=42.0
P<0.01
(h)MF
y=0.9x+18.55
N=18259
RMSEs=11.0
NSE=0.92
RMSEu=26.4
R=0.96
RMSE=28.6
P<0.01
(i)OSH
y=0.89x+17.95
N=22933
RMSEs=12.4
NSE=0.90
RMSEu=30.6
R=0.95
RMSE=33.0
P<0.01
(j)SAV
y=0.47x+117.96
N=12782
RMSEs=40.0
NSE=0.29
RMSEu=48.9
R=0.59
RMSE=63.2
P<0.01
(k)WSA
y=0.79x+37.42
N=14610
RMSEs=19.4
NSE=0.77
RMSEu=37.7
R=0.88
RMSE=42.4
P<0.01
(l)WET
y=0.8x+36.65
N=23317
RMSEs=21.2
NSE=0.66
RMSEu=55.4
R=0.82
RMSE=59.4
P<0.01
ERA5_Rd (W m²)
Obv_Rd (W m²)
Frequency

**Figure 3.** The scatter plot of downward solar radiation from ERA5-Land (ERA5_Rd) compared with local instruments measurements (Obv_Rd) under 12 IGBP land cover types: CRO (Croplands), CSH (Closed shrublands), DBF (Deciduous broadleaf forests), DNF (Deciduous needle leaf forests), EBF (Evergreen broadleaf forests), ENF (Evergreen needle leaf forests), GRA (Grasslands), MF (Mixed forests), OSH (Open shrublands), SAV (Savannas), WSA (Woody savannas), WET (Permanent wetlands). The red dotted line is the 1:1 line. N is the number of data points, NSE is Nash-Sutcliffe Efficiency, R is correlation coefficients, RMSE is Root Mean Square Error, RMSEs is systematic RMSE, and RMSEu is unsystematic RMSE. The Frequency denotes the probability density estimated through the KDE method with a Gaussian kernel, and it is then scaled to ensure that the maximum value of the probability density function equals 1. P is the P-Value for the Correlation Coefficient.

In Figure 3, ERA5_Rd exhibits optimal performance in DNF and MF, reflected by NSE and R values surpassing 0.9. In these land covers, the mean RMSEs stand at 11 W $m^{-2}$, mean RMSEu at 24.5 W $m^{-2}$, and mean RMSE at 26.9 W $m^{-2}$. However, its performance in SAV is notably subpar, characterized by an NSE of 0.29, an R of 0.59, highest RMSEs of 40 W $m^{-2}$, RMSEu of 48.9 W $m^{-2}$, and RMSE of 63.2 W $m^{-2}$. For ERA5_Rd, the mean RMSEs amount to 16 W $m^{-2}$, and the mean RMSEu is 34.8 W $m^{-2}$, suggesting that ERA5_Rd demonstrates high accuracy by effectively capturing the systematic variation in Obv_Rd, as indicated by its relatively low RMSEs and RMSEu close to RMSE (Willmott et al., 1981) in most land covers, except for SAV. Specifically, we have annotated the figure to indicate that all Rd values derived from ERA5 exhibit very low P-values (<0.01). This indicates a statistically significant correlation between the input shortwave radiation from ERA5 and the local measurements.

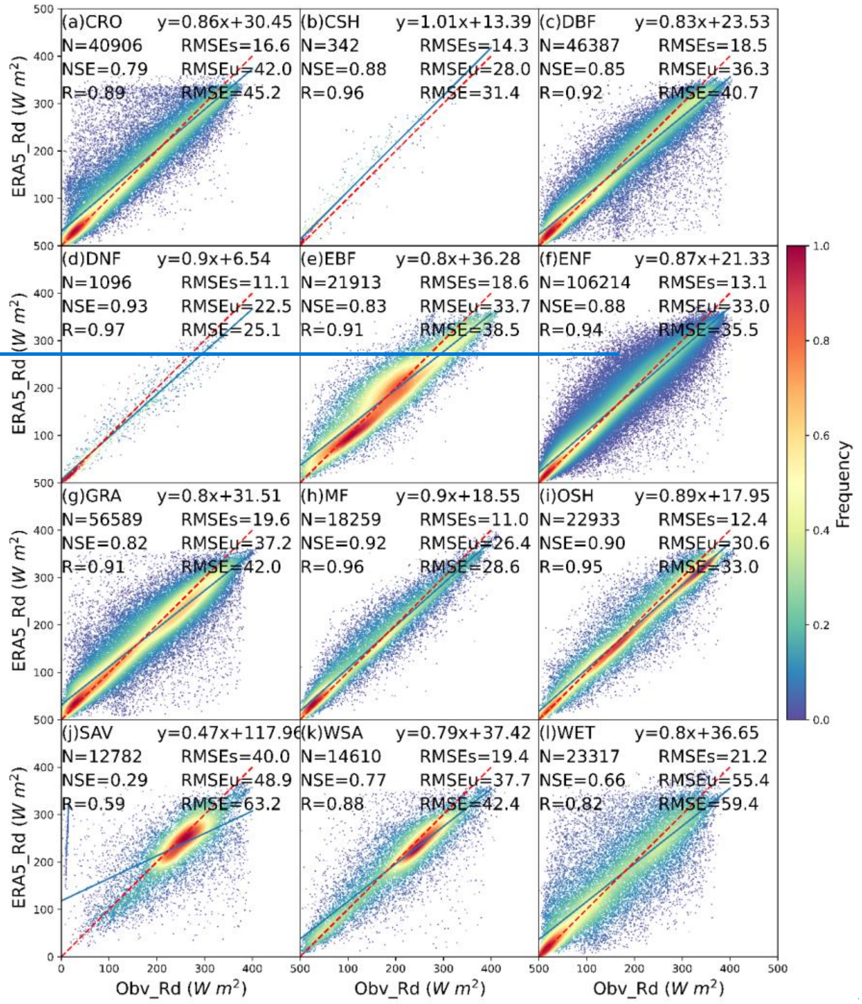


~~**Figure 3.** The scatter plot of downward solar radiation from ERA5-Land (ERA5_Rd) compared with local instruments measurements (Obv_Rd) under 12 IGBP land cover types: CRO (Croplands), CSH (Closed shrublands), DBF (Deciduous broadleaf forests), DNF (Deciduous needle leaf forests), EBF (Evergreen broadleaf forests), ENF (Evergreen needle leaf forests), GRA (Grasslands), MF (Mixed forests), OSH (Open shrublands), SAV (Savannas), WSA (Woody savannas), WET (Permanent wetlands). The red dotted line is the 1:1 line. N is the number of data points, NSE is Nash-Sutcliffe Efficiency, R is correlation coefficients, RMSE is Root Mean Square Error, RMSEs is systematic RMSE, and RMSEu is unsystematic RMSE.~~

Several factors come into play in understanding the disparities in performance in downward solar radiation of ERA5 (ERA5_Rd) across different land cover types. In regions characterized by denser forests, such as DNF and MF, ERA5_Rd's superior performance may be attributed to the lower density of ground-based meteorology stations (DNF, N = 1096) and the relatively uniform subsurface and canopy coverage in MF, facilitating a more accurate representation in the ERA5 radiative transfer model. Conversely, savannas present unique challenges due to sparse vegetation and flat terrain, influencing sunlight transmission dynamics (Yang and Friedl, 2003). Land-use changes, including farming and urban development, further complicate the accuracy of sunlight transmission (Wang et al., 2014; Zhang et al., 2022). Additionally, factors like aerosols from natural or anthropogenic sources contribute to data variations ~~(Naud et al., 2014; Wang et al., 2021).~~(Naud et al., 2014; Wang et al., 2021b). The inaccuracies in accounting for the rainy season, leading to increased cloud cover and rainfall in savannas, contribute to ERA5_Rd's limitations (Jiang et al., 2020).

Our local scale evaluation, as demonstrated in Figure 3, supports our stance that this resolution disparity between MODIS Land product at 0.05° and ERA5 data at 0.1° minimally impacts the final ET product's accuracy. This approach is consistent with the methodologies adopted in the studies by Huang et al. (2017, 2021, 2023), which effectively utilized MODIS land products at a 0.05° resolution in conjunction with downward shortwave radiation data at a 0.1° resolution from the China Meteorology Forcing Dataset. Such precedents underscore the feasibility of integrating these resolutions for ET estimation, bolstering our confidence in the methodological integrity of our study despite the noted resolution differences.

Figure 4 depicts scatter plots illustrating the comparison between the estimated air temperature using the VI-$T_S$ method (VISEA_Ta) and local meteorological measurements (Obv_Ta). The analysis reveals that VISEA_Ta generally aligns with Obv_Ta, exhibiting NSE values ranging from -0.22 (MF) to 0.82 (OSH), R values ranging from 0.44 (MF) to 0.97 (DNF), and RMSE values ranging from 5.7 K (WSA) to 11.2 K (MF). Particularly noteworthy is VISEA_Ta's outstanding performance at OSH (NSE = 0.82, R = 0.93, RMSE = 6.6 K), WSA (NSE = 0.79, R = 0.92, RMSE = 5.7 K) and GRA (NSE = 0.66, R = 0.88, RMSE = 6.8 K).

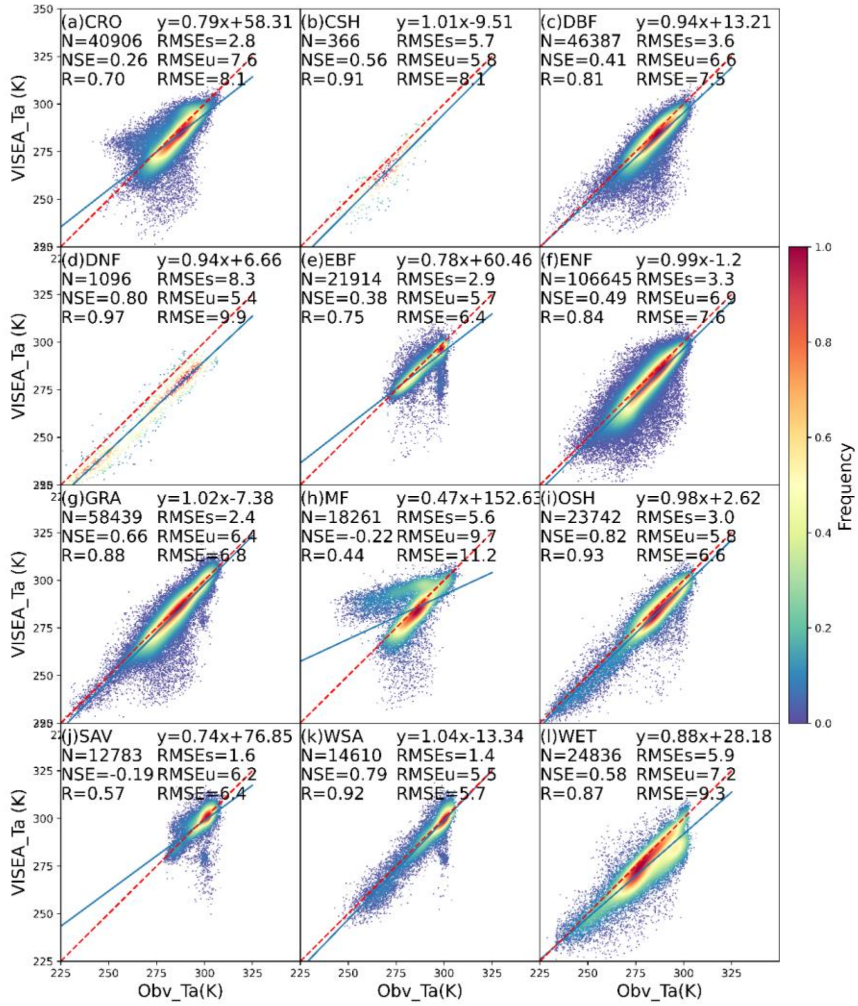


**Figure 4.** The scatter plot of daily air temperature simulated by VISEA (VISEA_Ta) compared with local instruments measurements (Obv_Ta) under 12 IGBP land cover types: CRO (Croplands), CSH (Closed shrublands), DBF (Deciduous broadleaf forests), DNF (Deciduous needle leaf forests), EBF (Evergreen broadleaf forests), ENF (Evergreen needle leaf forests), GRA (Grasslands), MF (Mixed forests), OSH (Open shrublands), SAV (Savannas), WSA (Woody savannas), WET (Permanent wetlands). The red dotted line is the 1:1 line. N is the number of data points, NSE is Nash-Sutcliffe Efficiency, R is correlation coefficients, RMSE is Root Mean Square Error, RMSEs is systematic RMSE, and RMSEu is unsystematic RMSE. The frequency denotes the probability density estimated through the Kernel Density Estimation, KDE method with a Gaussian kernel, and it is then scaled to ensure that the maximum value of the probability density function equals 1.

Conversely, its least satisfactory performance is evident at MF (NSE = -0.22, R = 0.44, RMSE = 11.2 K), SAV (NSE = -0.19, R = 0.57, RMSE = 6.4 K), and CRO (NSE = 0.26, R = 0.70, RMSE = 8.1 K). The RMSEs are lower than RMSEu in most land cover sites, except in DNF. Despite VISEA_Ta displaying a high NSE of 0.8 and R of 0.97 at DNF, it exhibits higher RMSEs (8.3 K) compared to RMSEu (5.4 K), indicating a systematic underestimation of VISEA_Ta at DNF.

**带格式的:** 缩进: 首行缩进:  0 字符

As detailed in Section 2.4, the VI-Ts method relies on a negative correlation between vegetation coverage (VI) and land surface temperature (Ts), ideally suited for cases with significant VI and Ts differences. However, for land cover types like DNF and MF situated in temperate regions with distinct seasons and cool to cold climates, the assumed negative correlation breaks down. In these regions, the positive correlation between VI and Ts, driven by vegetation growth proportional to rising Ts, results in the failure of the VI-Ts method. The challenges persist in SAV, where the VI-Ts method encounters difficulties during both dry and wet seasons. In the dry season, the method falters due to the prevalence of bare soil, resulting in VI values approaching zero and homogeneous high Ts values. Conversely, the wet season presents challenges with both VI and Ts exhibiting relatively high values and limited variances between grid cells, ultimately undermining the accuracy of VISEA_Ta estimation.

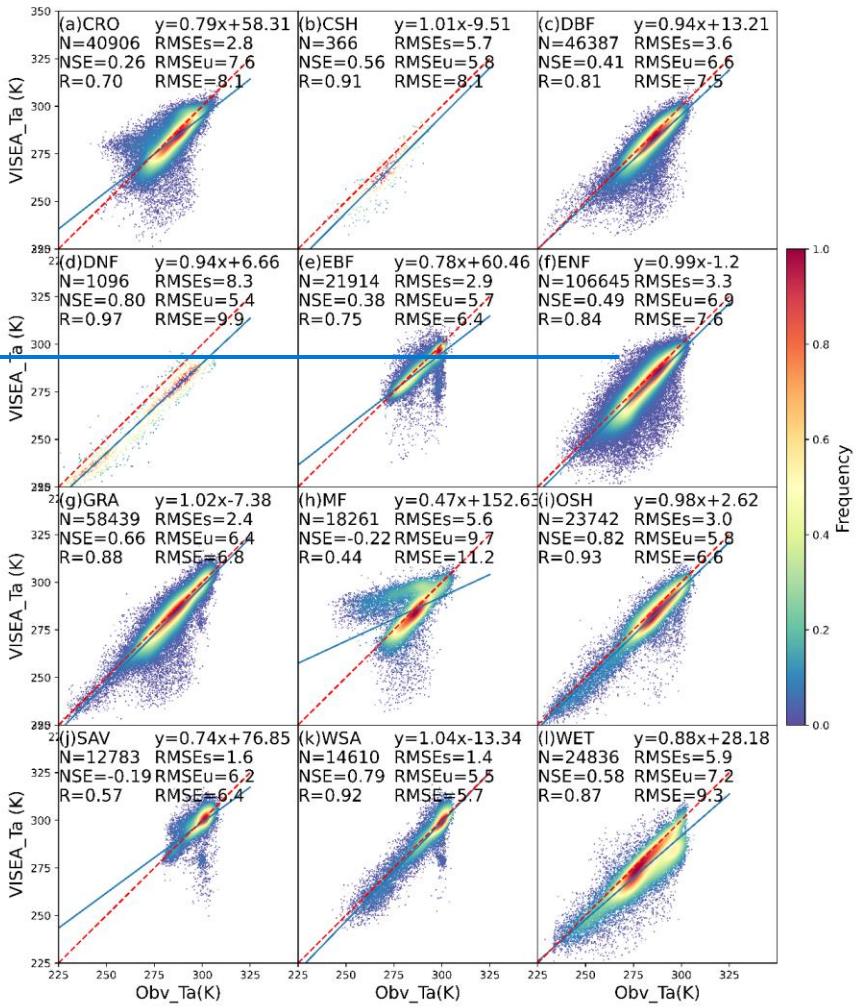


~~**Figure 4.** The scatter plot of daily air temperature simulated by VISEA (VISEA_Ta) compared with local instruments measurements (Obv_Ta) under 12 IGBP land cover types: CRO (Croplands), CSH (Closed shrublands), DBF (Deciduous broadleaf forests), DNF (Deciduous needle leaf forests), EBF (Evergreen broadleaf forests), ENF (Evergreen needle leaf forests), GRA (Grasslands), MF (Mixed forests), OSH (Open shrublands), SAV (Savannas), WSA (Woody savannas), WET (Permanent wetlands). The red dotted line is the 1:1 line. N is the number of data points, NSE is Nash-Sutcliffe Efficiency, R is correlation coefficients, RMSE is Root Mean Square Error, RMSEs is systematic RMSE, and RMSEu is unsystematic RMSE.~~

The simulated daily net radiation (VISEA_Rn) from VISEA is assessed against local meteorological measurements (Obv_Rn) in Figure 5. In contrast to the satisfactory performance of ERA5_Rd in Figure 3, VISEA_Rn exhibits more notable discrepancies, characterized by significant underestimation compared to Obv_Rn. This is reflected in the mean NSE of 0.49, mean R of 0.74, and mean RMSE of 43.3 W $m^{-2}$.

**带格式的:** 段落间距段后: 1 行, 行距: 1.5 倍行距

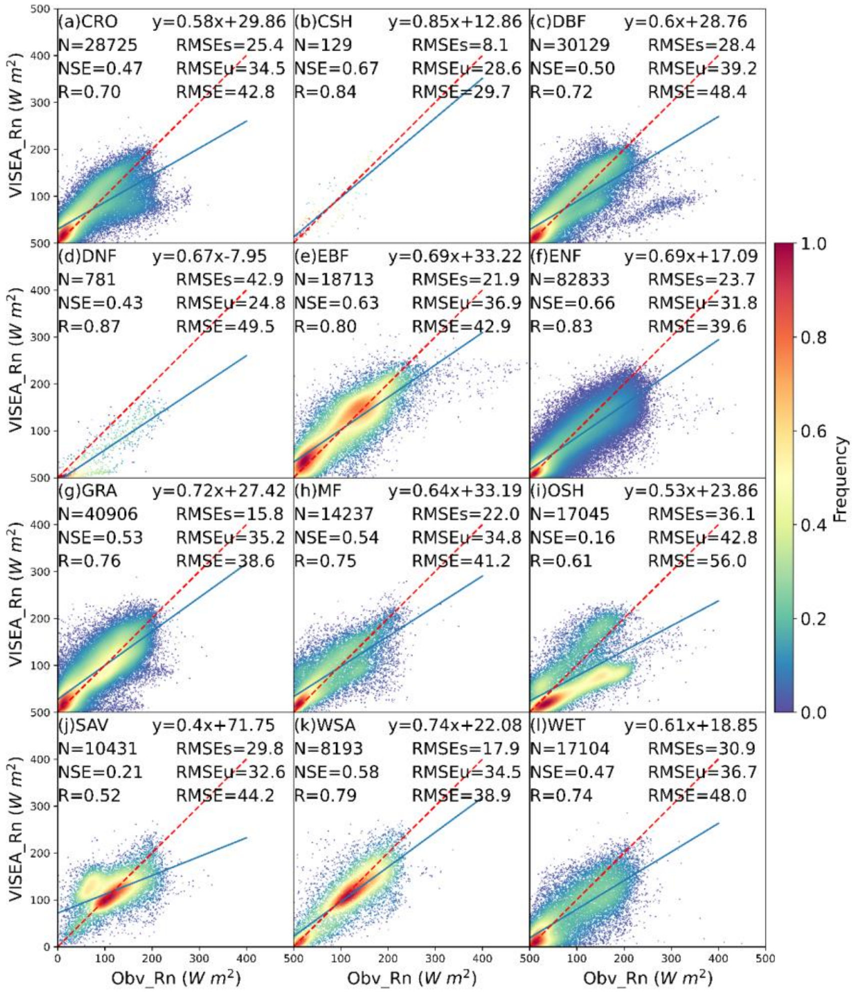


~~**Figure 5.** The scatter plot of daily net radiation simulated by VISEA (VISEA_Rn) compared with local instruments measurements (Obv_Rn) under 12 IGBP land cover types: CRO (Croplands), CSH (Closed shrublands), DBF (Deciduous broadleaf forests), DNF (Deciduous needle leaf forests), EBF (Evergreen broadleaf forests), ENF (Evergreen needle leaf forests), GRA (Grasslands), MF (Mixed forests), OSH (Open shrublands), SAV (Savannas), WSA (Woody savannas), WET (Permanent wetlands). The red dotted line is the 1:1 line. N is the number of data points, NSE is Nash-Sutcliffe Efficiency, R is correlation coefficients, RMSE is Root Mean Square Error, RMSEs is systematic RMSE, and RMSEu is unsystematic RMSE.~~

Specifically, VISEA_Rn demonstrates good accuracy in certain land cover types, including CHS with an NSE of 0.67, R of 0.84, and RMSE of 29.7 W m$^{-2}$, EBF with an NSE of 0.63, R of 0.8, and RMSE of 42.9 W m$^{-2}$, and ENF with an NSE of 0.66, R of 0.83, and RMSE of 39.6 W m$^{-2}$. However, its performance diminishes notably at OSH, where it records an NSE of 0.16, R of 0.61, and RMSE of 56 W m$^{-2}$, as well as in SAV, with an NSE of 0.21, R of 0.52, and RMSE of 44.2 W m$^{-2}$.

While VISEA_Rn appears to have lower accuracy compared to ERA5_Rd, in the majority of land cover types, the RMSEs are smaller than RMSEu, with mean RMSEs of 25.2 W m$^{-2}$ and mean RMSEu of 34.3 W m$^{-2}$. Moreover, the RMSEu of 43.3 W m$^{-2}$ is almost the same as the RMSE. These findings suggest that VISEA_Rn demonstrates fewer systematic biases, with unsystematic RMSEu contributing the most to the overall RMSE.

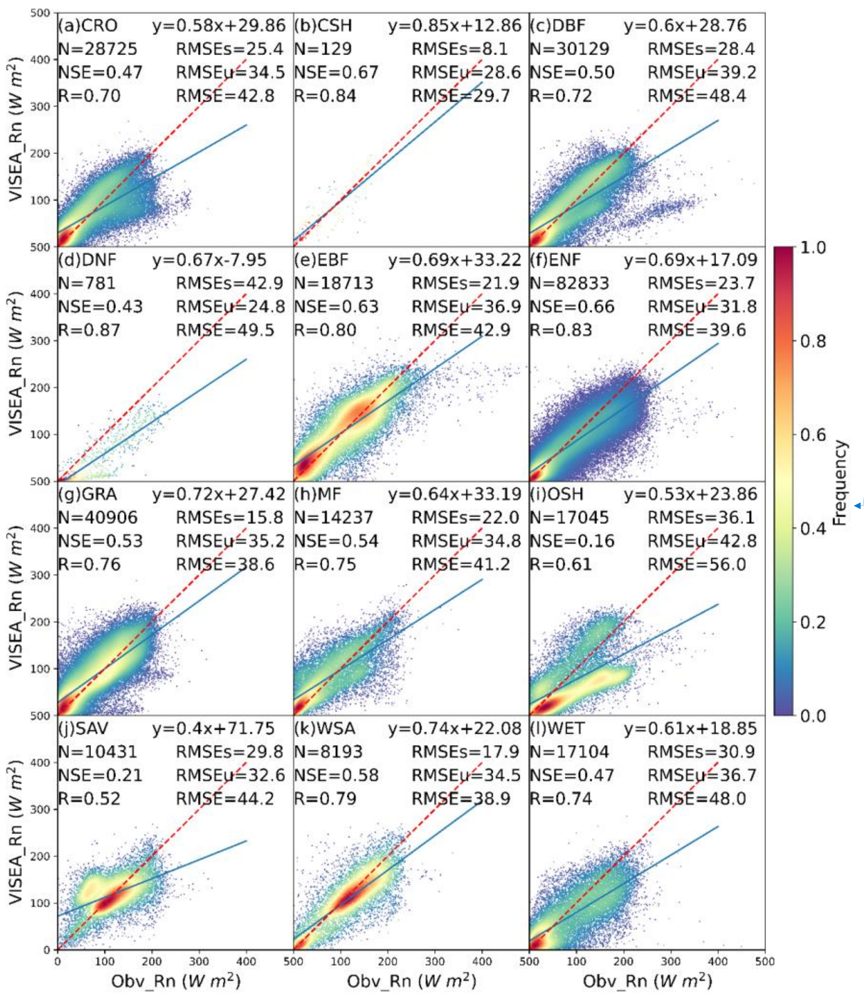


**带格式的:** 段落间距段后: 1 行, 行距: 1.5 倍行距

**Figure 5.** The scatter plot of daily net radiation simulated by VISEA (VISEA_Rn) compared with local instruments measurements (Obv_Rn) under 12 IGBP land cover types: CRO (Croplands), CSH (Closed shrublands), DBF (Deciduous broadleaf forests), DNF (Deciduous needle leaf forests), EBF (Evergreen broadleaf forests), ENF (Evergreen needle leaf forests), GRA (Grasslands), MF (Mixed forests), OSH (Open shrublands), SAV (Savannas), WSA (Woody savannas), WET (Permanent wetlands). The red dotted line is the 1:1 line. N is the number of data points, NSE is Nash-Sutcliffe Efficiency, R is correlation coefficients, RMSE is Root Mean Square Error, RMSEs is systematic RMSE, and RMSEu is unsystematic RMSE. The frequency denotes the probability density estimated through the Kernel Density Estimation, KDE method with a Gaussian kernel, and it is then scaled to ensure that the maximum value of the probability density function equals 1.

In the context of VISEA_Rn, a consistent pattern of approximately 30% underestimation in net radiation across various land cover types raises noteworthy discussions. This systematic discrepancy could be linked to the disparity in vegetation coverage between the observed sites' footprint and the mean vegetation coverage of the 0.05° × 0.05° grid cell. Specifically, the lower albedo within the footprint, compared to the grid cell's average albedo (as expressed by Eq. ~~20~~14, contributes to the underestimation of Obv_Rn. This is particularly evident in OSH, where the vegetation coverage within the footprint significantly exceeds the mean vegetation coverage of the grid cell (<0.2 compared to >0.5).

Additionally, factors such as the bias in ERA5_Rd (refer to Fig. 3, j) and VISEA_Ta (refer to Fig. 4, j) contribute to the underestimation of VISEA_Rn in SAV. Moreover, a substantial 50% underestimation in DNF results from the underestimated VISEA_Ta (refer to Fig. 4, d), leading to a subsequent underestimation of downward long-wave radiation. Unpacking these intricacies sheds light on the nuanced interplay of variables influencing the observed underestimation trends in VISEA_Rn across diverse land cover types.

Figure 6 illustrates scatter plots of daily evapotranspiration (ET) simulated by VISEA (VISEA_ET) against eddy covariance measurements obtained from 149 flux tower sites (Obv_ET) across 12 IGBP land cover types. The scatter plots of VISEA_ET reveal a dispersed distribution, as evidenced by an average NSE of -0.08, average R of 0.56, and average RMSE of 1.4 mm day$^{-1}$. Notably, VISEA_ET tends to underestimate daily ET across most land cover types.

Among the 12 land cover types, VISEA_ET exhibits the highest accuracy in DNF, with an NSE of 0.4, an R of 0.82, and an RMSE of 0.9 mm day$^{-1}$. It was closely followed by GRA, with NSE values of 0.26, R values of 0.65, and RMSE values of 1.3 mm day$^{-1}$. However, for CRO, ENF, and WET land cover types, the NSE values, although above 0, are close to 0 (mean NSE of 0.11), with a mean R of 0.53 and a mean RMSE of 1.3 mm day$^{-1}$. In the remaining land cover types, particularly in OSH and SAV, VISEA_ET appears to struggle in aligning with local measurements, resulting in NSE values of -0.57 and -0.51, R values of 0.31 and 0.36, and RMSE values of 1.2 mm day$^{-1}$ and 1.7 mm day$^{-1}$, respectively.

**带格式的:** 缩进: 首行缩进: 0 厘米

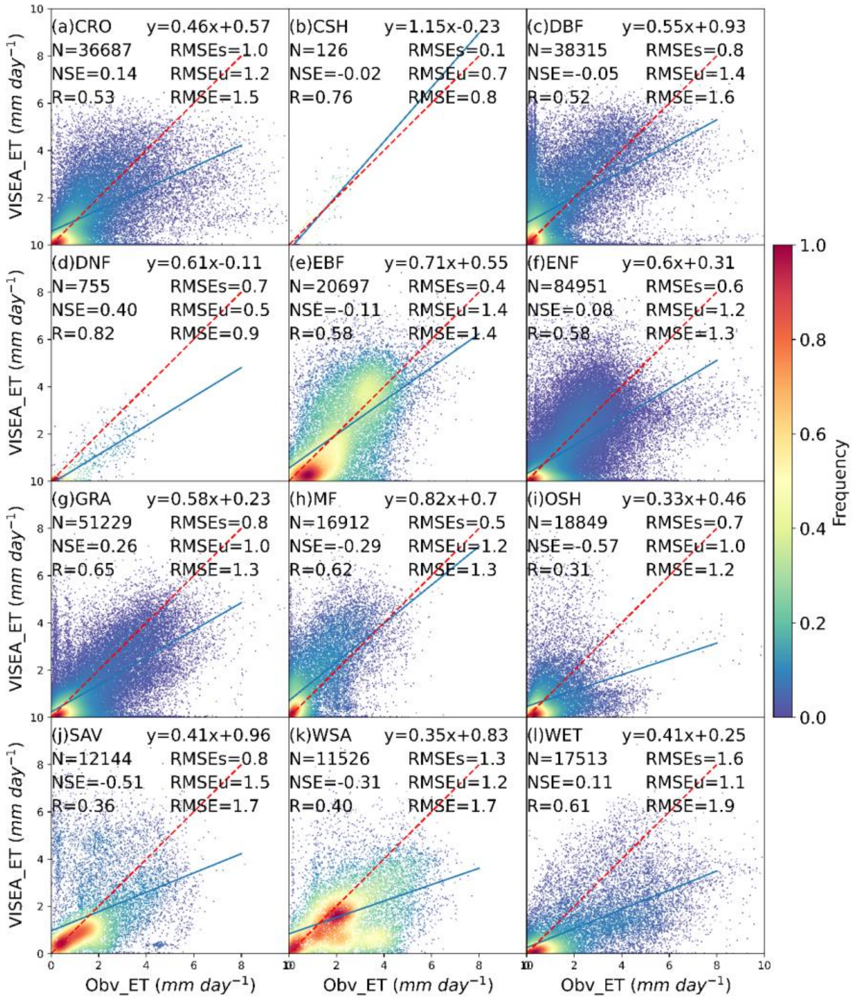


~~**Figure 6.** The scatter plot of daily ET simulated by VISEA (VISEA_ET) compared with local instruments measurements (Obv_ET) under 12 IGBP land cover types: CRO (Croplands), CSH (Closed shrublands), DBF (Deciduous broadleaf forests), DNF (Deciduous needle leaf forests), EBF (Evergreen broadleaf forests), ENF (Evergreen needle leaf forests), GRA (Grasslands), MF (Mixed forests), OSH (Open shrublands), SAV (Savannas), WSA (Woody savannas), WET (Permanent wetlands). The red dotted line is the 1:1 line. N is the number of data points, NSE is Nash-Sutcliffe Efficiency, R is correlation coefficients, RMSE is Root Mean Square Error, RMSEs is systematic RMSE, and RMSEu is unsystematic RMSE.~~

As the evaluation of daily VISEA_ET with observed ET, Obv_ET, at CRO and WET, the bias mainly come from the bias in ERA5_Rd (the third highest RMSE of 45.2 W $m^{-2}$ and second highest RMSE of 59.4 W $m^{-2}$) (Fig. 3, a and l). In ENF, the biases primarily could by the disability of VISEA_ET

**带格式的:** 首行缩进: 0 字符

to capturing the Obv_ET under a cold climate, with low net radiation estimation (Fig. 5, f), and air temperature (Fig. 4, f). For OSH, the bias mainly arises from the poor estimation of VISEA_Rn, which has the lowest NSE of 0.16 and highest RMSE of 56 W $m^{-2}$ (Fig. 5, i). The bias of VISEA_ET in SAV is a result of the combined biases in ERA5_Rd (the lowest NSE and R of 0.29 and 0.59, respectively, and the highest RMSE of 63.2 W $m^{-2}$), VISEA_Ta (the second lowest NSE and R of -0.19 and 0.57 , respectively).

带格式的: 缩进: 首行缩进: 0 厘米

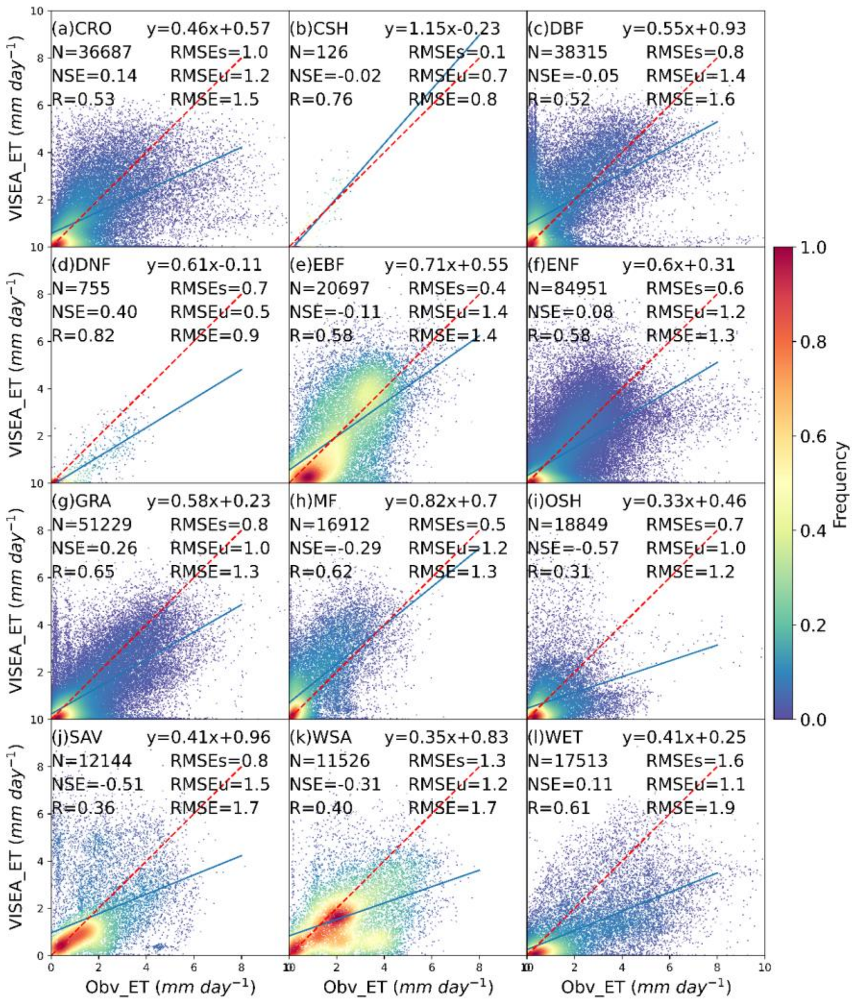

**Figure 6.** The scatter plot of daily ET simulated by VISEA (VISEA_ET) compared with local instruments measurements (Obv_ET) under 12 IGBP land cover types: CRO (Croplands), CSH (Closed shrublands), DBF (Deciduous broadleaf forests), DNF (Deciduous needle leaf forests), EBF (Evergreen broadleaf forests), ENF (Evergreen needle leaf forests), GRA (Grasslands), MF (Mixed forests), OSH (Open shrublands), SAV (Savannas), WSA (Woody savannas), WET (Permanent wetlands). The red dotted line is the 1:1 line. N is the number of data points, NSE is Nash-Sutcliffe Efficiency, R is correlation coefficients, RMSE is Root Mean Square Error, RMSEs is systematic RMSE, and RMSEu is unsystematic RMSE. The frequency denotes the probability density estimated through the Kernel Density Estimation, KDE method with a Gaussian kernel, and it is then scaled to ensure that the maximum value of the probability density function equals 1.

In Figure 7, we utilized Taylor diagrams (Taylor, 2001) to evaluate the performances of six global gridded monthly ET products with simulated ET from VISEA (a), GLEAM (b), ~~GBAF~~FLUXCOM (c), AVHRR (d), MOD16 (e), and PML (f). ~~The~~ Table 3 lists statistical ~~values,~~metrics including correlation coefficient (CC), bias, RMSE, RMSEu, RMSEs, and ~~NSE are presented in Table 3. In contrast to the daily evaluation of VISEA, the assessment on a monthly scale revealed significant performance metrics for VISEA, featuring a robust mean correlation coefficient (CC) of 0.69, a mean~~ Nash-Sutcliffe Efficiency (NSE) ~~of 0.25,~~across different vegetation types and ~~the highest mean Ratio of 0.94. On the downside, VISEA exhibited the highest mean bias, signifying an underestimation of -9.7 mm month$^{-1}$~~their mean values. The vegetation types include Croplands (CRO), Closed Shrublands (CSH), Deciduous Broadleaf Forest (DBF), Deciduous Needleleaf Forest (DNF), Evergreen Broadleaf Forest (EBF), Evergreen Needleleaf Forest (ENF), Grasslands (GRA), Mixed Forests (MF), Open Shrublands (OSH), Savannas (SAV), Woody Savannas (WSA), Wetlands (WET), and ~~a moderate mean RMSE of 31.5 mm month$^{-1}$. Comparatively, MOD16 has slightly better performance than VISEA with the second highest CC of 0.72 and higher NSE of 0.41, lower bias of -8.3 mm month$^{-1}$ and RMSE of 28.7 mm month$^{-1}$.~~an overall mean (MEAN).

~~In contrast, GLEAM and PML stood out as top performers among all products. GLEAM displays the second-highest CC of 0.71, a mean NSE of 0.39 and the lowest mean bias at 2.3 mm month$^{-1}$. While, it also exhibited the highest mean RMSE of 31.5 mm month$^{-1}$ among the products. On the other hand, PML achieved the highest mean CC of 0.75 and the highest NSE of 0.49 coupled with the lowest RMSE at 25.9mm month$^{-1}$ affirming its relatively accurate estimations. GBAF and AVHRR exhibit a higher degree of disagreement with the observed data compared to the other ET products. GBAF presents the lowest mean CC of 0.62, the second lowest NSE of 0.16, and an RMSE of 30.58 mm month$^{-1}$, while it has the second lowest mean bias of -4.3 mm month$^{-1}$, providing valuable insights into its performance characteristics. On the other hand, AVHRR records the lowest NSE of 0.12, second lowest CC of 0.69 and the highest RMSE of 31.5 mm month$^{-1}$.~~

656

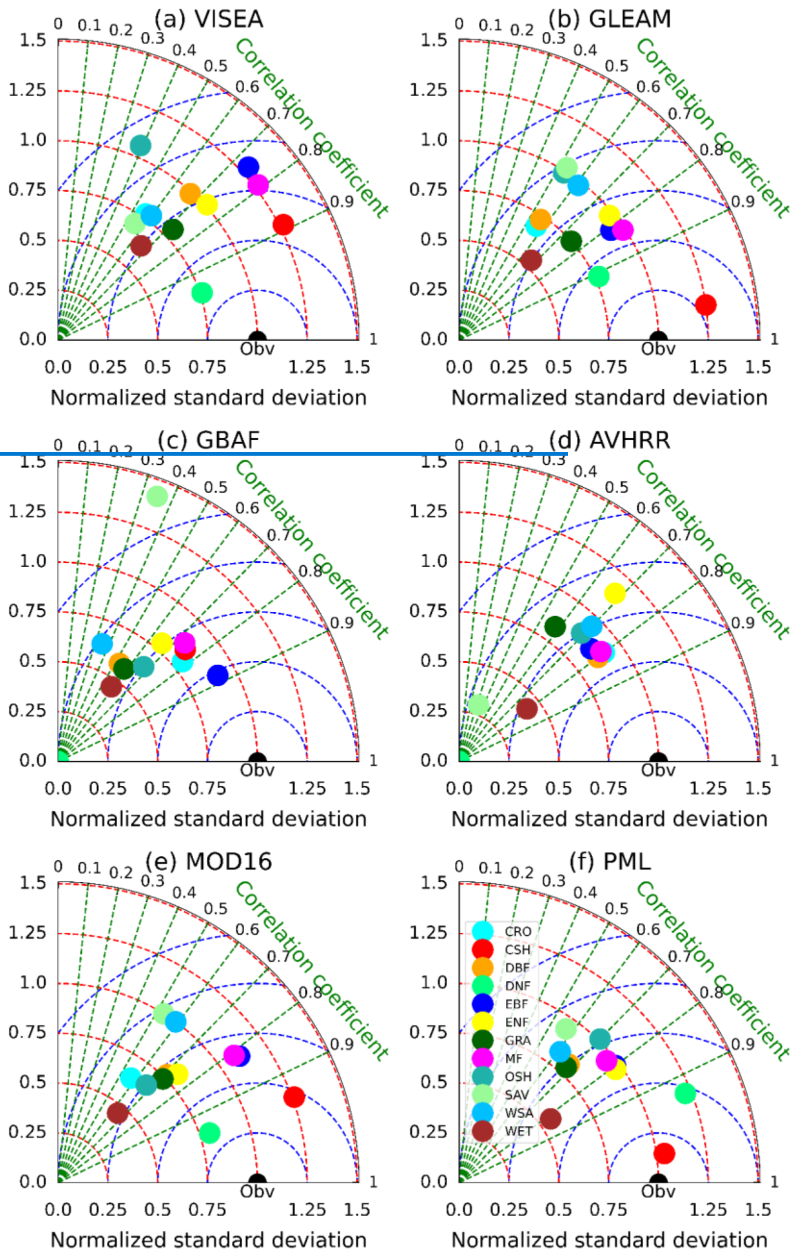

(a) VISEA
(b) GLEAM
(c) GBAF
(d) AVHRR
(e) MOD16
(f) PML
Correlation coefficient
Normalized standard deviation
Obv
CRO
CSH
DBF
DNF
EBF
ENF
GRA
MF
OSH
SAV
WSA
WET

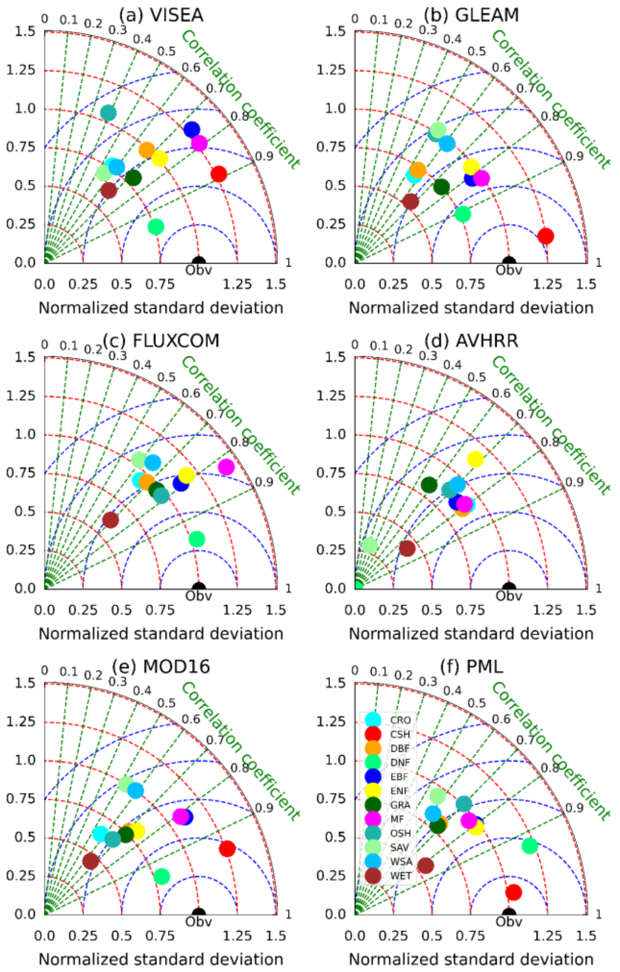


**Figure 7.** Taylor Diagrams comparing monthly measurements of (a) VISEA, GLEAM (b), ~~GBAF~~FLUXCOM (c), AVHRR (d), MOD16 (e), and PML (f) with 150 flux towers (labeled as Obv) in different IGBP land cover types. The diagrams display the Normalized Standard Deviation (represented by red circles), Correlation Coefficient (shown as green lines), and Centred Root-Mean-Square (depicted as blue circles).

**Table 3.** Statistical variables of six ET Products – CC (Correlation Coefficient), Ratio (the ratio of the standard deviations of simulated ET and flux tower measurements), Bias, RMSE, RMSEu, RMSEs, and NSE.

| | | CRO | CSH | DBF | DNF | EBF | ENF | GRA | MF | OSH | SAV | WSA | WET | MEAN |
|---|---|---|---|---|---|---|---|---|---|---|---|---|---|---|
| **VISEA** | CC | 0.57 | 0.89 | 0.67 | 0.95 | 0.74 | 0.74 | 0.72 | 0.79 | 0.39 | 0.55 | 0.6 | 0.66 | 0.69 |
| | Ratio | 0.77 | 1.27 | 0.99 | 0.76 | 1.29 | 1.01 | 0.8 | 1.27 | 1.06 | 0.7 | 0.78 | 0.63 | 0.94 |
| | Bias | -14.16 | -1.27 | 3.9 | -19.06 | 1.37 | -12.84 | -13.47 | 1.53 | -6.83 | -0.45 | -23.14 | -31.98 | -9.70 |

| | | | | | | | | | | | | | | |
|---|---|---|---|---|---|---|---|---|---|---|---|---|---|---|
| | RMSE | 39.4 | 12.5 | 34 | 22.1 | 30.4 | 28.5 | 32 | 23.3 | 30.4 | 32.5 | 41.2 | 51.6 | 31.49 |
| | RMSEU | 27.4 | 12.1 | 30.7 | 7.4 | 30.4 | 23.8 | 23.1 | 23.2 | 25.4 | 22.5 | 25.8 | 25.4 | 23.10 |
| | RMSES | 28.3 | 3.1 | 14.5 | 20.8 | 2.2 | 15.7 | 22.2 | 1.5 | 16.8 | 23.5 | 32.1 | 44.9 | 18.80 |
| | NSE | 0.18 | 0.64 | 0.34 | 0.45 | 0.24 | 0.33 | 0.41 | 0.38 | -0.36 | 0.28 | 0.01 | 0.08 | 0.25 |
| **GLEAM** | CC | 0.56 | 0.99 | 0.56 | 0.91 | 0.81 | 0.77 | 0.75 | 0.83 | 0.53 | 0.53 | 0.61 | 0.67 | 0.71 |
| | Ratio | 0.69 | 1.25 | 0.73 | 0.77 | 0.94 | 0.98 | 0.75 | 0.99 | 0.99 | 1.02 | 0.98 | 0.54 | 0.89 |
| | Bias | -5.68 | 10.71 | -3.55 | -6.12 | 3.41 | 2.34 | -2.01 | 10.67 | 4.44 | -7.99 | -17 | -16.26 | -~~2.25~~1.66 |
| | RMSE | 36.8 | 12.1 | 35.8 | 14.6 | 21.4 | 23.8 | 27.6 | 20.2 | 25.6 | 38.4 | 39.8 | 43.3 | 28.28 |
| | RMSEU | 24.6 | 3.2 | 25.4 | 9.6 | 19.4 | 22.0 | 20.7 | 16.3 | 21.9 | 33.2 | 31.9 | 21.4 | 20.80 |
| | RMSES | 27.3 | 11.6 | 25.3 | 10.9 | 9.1 | 9 | 18.2 | 11.9 | 13.1 | 19.3 | 23.7 | 37.7 | 18.~~92~~09 |
| | NSE | 0.29 | 0.~~66~~60 | 0.28 | 0.77 | 0.62 | 0.53 | 0.57 | 0.53 | 0.03 | -0.01 | 0.06 | 0.34 | 0.~~39~~38 |
| **~~GBAF~~FLUXCOM** | CC | 0.~~786~~6 | 0.~~75~~98 | 0.~~536~~9 | -0.95 | 0.~~887~~9 | 0.~~667~~8 | 0.~~58~~75 | 0.~~73~~83 | 0.~~677~~8 | 0.~~35~~59 | 0.~~35~~65 | 0.~~58~~69 | 0.~~62~~76 |
| | Ratio | 0.894 | ~~0.85~~1.76 | 0.~~589~~6 | -1.04 | ~~0.91~~1.12 | ~~0.79~~1.18 | 0.~~57~~97 | ~~0.87~~1.42 | 0.~~649~~7 | 1.~~42~~04 | ~~0.63~~1.08 | 0.~~46~~62 | ~~0.77~~1.09 |
| | Bias | ~~3.487~~.22 | ~~18.25~~23.49 | ~~3.53~~17.57 | -2.26 | -~~1.55~~6.29 | -~~7.95~~6.40 | -~~12.51~~6.91 | ~~14.08~~21.02 | ~~1.96~~10.04 | -~~10.02~~0.74 | -~~25.08~~9.75 | -~~31.66~~14.04 | -~~4.32~~6.14 |
| | RMSE | ~~22.53~~5.8 | ~~21.82~~7.9 | ~~35.93~~6.7 | -9.9 | ~~16.32~~5.2 | 26.~~2~~7 | ~~37.13~~0.0 | 31.9~~24~~.2 | ~~21~~198 | ~~33.73~~5.5 | ~~43.13~~7.8 | ~~53.84~~1.7 | ~~30.58~~29.91 |
| | RMSEU | ~~17.83~~1.0 | ~~10~~5.8 | ~~20.82~~8.9 | -9.7 | ~~14.72~~4.1 | ~~19.42~~5.8 | ~~20~~26.8 | ~~16.72~~3.5 | ~~13~~158 | ~~30.23~~2.3 | ~~21.23~~4.3 | 24.2~~2~~0 | ~~18.60~~23.52 |
| | RMSES | ~~13.81~~8.0 | ~~19.42~~7.3 | ~~29.32~~2.6 | -2.3 | -7.5 | ~~17~~7 | ~~31.21~~3.4 | ~~17.52~~1.6 | ~~16~~119 | ~~15.11~~4.8 | ~~37.51~~5.8 | ~~50~~33.9 | ~~24.84~~16.34 |
| | NSE | 0.~~63~~2 | ~~0.49~~-1.14 | 0.~~272~~3 | -0.88 | 0.~~774~~8 | 0.~~374~~2 | 0.~~25~~48 | -0.~~26~~17 | 0.~~444~~3 | -~~1.21~~0.14 | -0.~~46~~17 | -0.~~03~~40 | 0.~~16~~22 |
| **AVHRR** | CC | 0.8 | _ | 0.8 | _ | 0.76 | 0.68 | 0.58 | 0.79 | 0.69 | 0.32 | 0.7 | 0.79 | 0.69 |
| | Ratio | 0.91 | _ | 0.87 | _ | 0.87 | 1.15 | 0.83 | 0.9 | 0.89 | 0.3 | 0.95 | 0.43 | 0.81 |
| | Bias | -1.15 | _ | 5.96 | _ | 5.24 | -2.73 | -7.04 | 0.16 | -2.41 | -47.83 | -0.42 | -25.32 | -7.55 |
| | RMSE | 23.6 | _ | 26.1 | _ | 23.3 | 31 | 36 | 18.8 | 22.1 | 54.7 | 33.2 | 46.6 | 31.54 |
| | RMSEU | 21.2 | _ | 22 | _ | 19.5 | 29.8 | 27.9 | 16.6 | 18.8 | _ | 29.8 | 14.6 | 22.24 |
| | RMSES | 10.4 | _ | 14.1 | _ | 12.7 | 8.4 | 22.7 | 8.7 | 11.6 | 54.2 | 14.6 | 44.2 | 20.16 |
| | NSE | 0.63 | _ | 0.61 | _ | 0.54 | 0.23 | 0.24 | 0.62 | 0.43 | -2.79 | 0.42 | 0.29 | 0.12 |
| **MOD16** | CC | 0.57 | 0.94 | 0.71 | 0.95 | 0.82 | 0.74 | 0.71 | 0.81 | 0.67 | 0.53 | 0.59 | 0.65 | 0.72 |
| | Ratio | 0.64 | 1.26 | 0.77 | 0.8 | 1.11 | 0.81 | 0.74 | 1.09 | 0.66 | 1 | 1 | 0.46 | 0.86 |
| | Bias | -7.88 | -14.03 | 5.79 | -4.07 | -7.17 | -4.51 | -5.05 | 4.09 | -6.41 | -16.01 | -23.76 | -21.07 | -8.34 |
| | RMSE | 36.9 | 16.7 | 30.7 | 11.1 | 23.4 | 24.3 | 29.6 | 19.4 | 20.4 | 40.4 | 44.3 | 47.2 | 28.70 |
| | RMSEU | 23 | 8.4 | 23 | 7.4 | 22 | 19.3 | 21.7 | 18.7 | 12.8 | 32.4 | 33.3 | 18.8 | 20.07 |
| | RMSES | 28.8 | 14.4 | 20.3 | 8.2 | 7.8 | 14.9 | 20.2 | 5.2 | 15.9 | 24.2 | 29.1 | 43.3 | 19.36 |
| | NSE | 0.28 | 0.24 | 0.48 | 0.87 | 0.55 | 0.52 | 0.5 | 0.57 | 0.39 | 0.12 | 0.14 | 0.23 | 0.41 |
| **PML** | CC | 0.68 | 0.99 | 0.68 | 0.93 | 0.8 | 0.81 | 0.68 | 0.77 | 0.7 | 0.57 | 0.61 | 0.82 | 0.75 |
| | Ratio | 0.8 | 1.04 | 0.81 | 1.22 | 0.98 | 0.97 | 0.79 | 0.96 | 1.01 | 0.94 | 0.83 | 0.56 | 0.91 |
| | Bias | -6.6 | -3 | -3.39 | 0.47 | -1.42 | -6.07 | -6.66 | -0.59 | 6.48 | -0.18 | -16.04 | -22.1 | -4.93 |
| | RMSE | 33.2 | 4.1 | 31.5 | 13.3 | 21.9 | 22.2 | 31.7 | 19.8 | 21.1 | 34.5 | 37.5 | 40.5 | 25.94 |
| | RMSEU | 25.6 | 2.8 | 25.1 | 12.7 | 20.5 | 20.1 | 24.1 | 18.2 | 18.6 | 29.5 | 27.1 | 17.3 | 20.13 |
| | RMSES | 21.1 | 3.1 | 19 | 3.9 | 7.8 | 9.6 | 20.6 | 7.7 | 9.9 | 17.8 | 26 | 36.6 | 15.26 |
| | NSE | 0.42 | 0.95 | 0.44 | 0.79 | 0.61 | 0.6 | 0.43 | 0.55 | 0.33 | 0.19 | 0.16 | 0.43 | 0.49 |

VISEA, with a mean correlation coefficient (CC) of 0.69, indicates moderate correlation across vegetation types but suffers from significant biases, notably in WET, with a mean bias of -9.7 mm month$^{-1}$. It also has the highest mean Root Mean Square Error (RMSE) at 31.5 mm month$^{-1}$ and a mean NSE of 0.25. MOD16 demonstrates a slightly better correlation with a mean CC of 0.72 and presents less variation in bias, resulting in a marginally lower mean RMSE of 28.7 mm month$^{-1}$ and a higher mean NSE of 0.41. AVHRR matches VISEA in mean CC at 0.69 but exhibits extreme biases, particularly in SAV, and achieves a comparable mean RMSE of 31.5 mm month$^{-1}$. However, its mean NSE of 0.12 is the lowest among the six products, suggesting its predictions are less reliable.

On the other hand, GLEAM, FLUXCOM, and PML show better agreements. GLEAM has a high mean CC of 0.71 with the lowest bias at -1.66 mm month$^{-1}$, indicating a consistent performance with a mean RMSE of 28.3 mm month$^{-1}$and a mean NSE of 0.38. FLUXCOM exhibits a higher mean CC of 0.76, suggesting better overall correlation, but with a higher mean bias of 6.1 mm month$^{-1}$, it hints at a tendency towards overestimation. The mean RMSE stands at 29.9 mm month$^{-1}$, with a mean NSE of 0.22. PML outperforms the others with the highest mean CC of 0.75 and the highest mean NSE of 0.49, indicating the strongest predictive accuracy. It also has the lowest mean RMSE at 25.9 mm month$^{-1}$, affirming its status as the most accurate ET estimation product among those evaluated.

Figure 8 illustrates the spatial distribution of the multi-year average ~~monthly precipitation data sourced from the Global Precipitation Climatology Centre (~~(a-g), the zonal mean (h) and inter-annual variation (i) of (a) GPCC~~) and the calculated evapotranspiration (ET) by various models, namely VISEA, GLEAM, GBAF, AVHRR, MOD16, and PML. Comparing these precipitation and ET products may seem incompatible; nevertheless, this section focuses on the distribution patterns of rainfall and ET rather than on their specific values.~~ (2001-2019), (b) VISEA (2001-2020), (c) GLEAM (2001-2020), (d) FLUXCOM (2001-2016), (e) AVHRR (2001-2006), (f) MOD16 (2001-2014) and (g) PML (2003-2018).

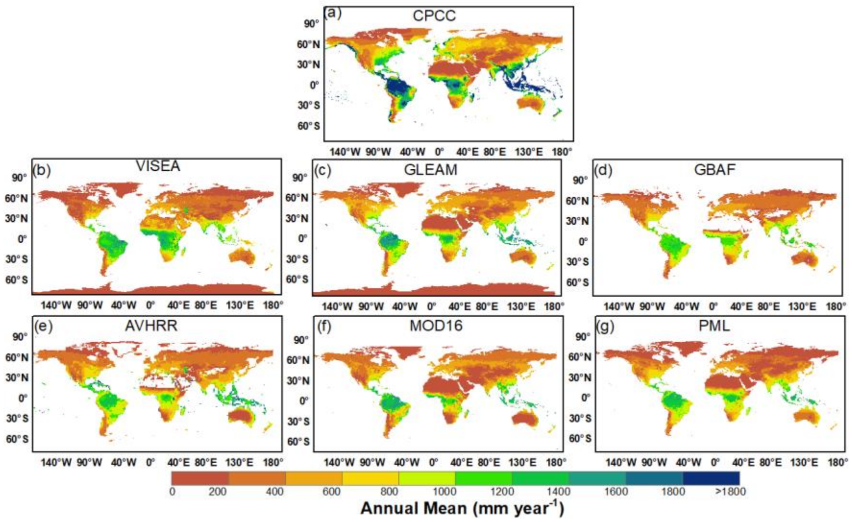

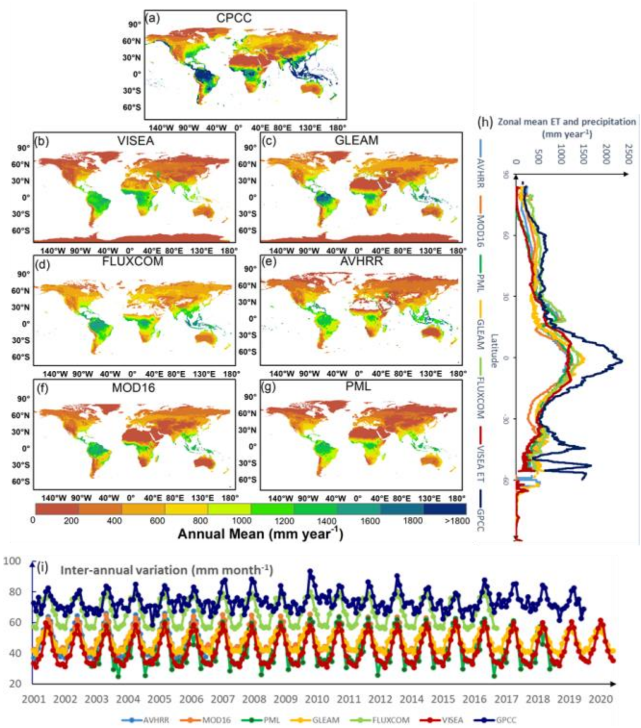


**Figure 8.** The spatial distribution of the multi-year average (~~2001-2019) for~~ a-g), the zonal mean (h) and inter-annual variation (i) of (a) GPCC (2001-2019~~),~~), (b) VISEA (2001-2020), (c) GLEAM (~~2003-2019~~2001-2020), (d) ~~GBAF~~FLUXCOM (2001-~~2008~~2016), (e) AVHRR (2001-2006), (f) MOD16 (2001-2014) and (g) PML (2003-2018).

~~All six of these ET products exhibit similar and coherent spatial ET distributions, which align with the precipitation distribution data from GPCC. The highest ET values (1,400 to 1,600 mm year$^{-1}$) are predominantly concentrated in equatorial low-latitude regions with the highest precipitation levels (1,600 to 1,800 mm year$^{-1}$). These regions include South America (Amazon Basin), Central Africa (Congo Basin), and Southeast Asia (encompassing Indonesia, Malaysia, parts of Thailand, and the Philippines), which are known for their tropical rainforest climates. These ET estimates align with the findings of Tapiador et al. (2012) and Panagos et al. (Panagos et al., 2017), who reported that the multi-year average annual precipitation is approximately 2,000 mm year$^{-1}$.~~

~~Conversely, areas categorized as barren land (BAR), including deserts such as Sahara, Arabian, Gobi, Kalahari, and large portions of Australia, as well as snow and ice (SI) areas like most parts of Canada, Russia, and the Qinghai-Tibet Plateau in China, where the growing seasons are short, typically falling below 400 mm year$^{-1}$. These areas are also characterized by the lowest annual precipitation, ranging from 200 to 400 mm year$^{-1}$ according to GPCC precipitation data mm year$^{-1}$. ET estimates for~~

~~other land cover types fall within this range, varying from 400 to 1,400 mm year$^{-1}$, in close alignment with the GPCC precipitation data, which falls between 600 to 1,600 mm year$^{-1}$.~~

~~Figure 9 presents the daily variations in ET from August 28$^{th}$, 2022, to September 1$^{st}$, 2022, within the Yangtze River Basin, along with the mean ET and Global Unified Gauge-Based Analysis of Daily Precipitation recorded during this period. According to a study by Zhang et al. (2023), the summer of 2022 witnessed a severe drought within the Yangtze River Basin. This drought commenced in July, gradually relenting in late August and early September. Figure 9 visually represents the drought severity, highlighting extremely low ET levels (below 0.2 mm day$^{-1}$) across most of the basin on August 28$^{th}$, 2022. Subsequently, on August 29$^{th}$, 2022, an upsurge in precipitation resulted in a corresponding increase in ET (exceeding 0.8 mm day$^{-1}$) throughout the majority of the basin, as depicted in subfigures (b)-(e).~~

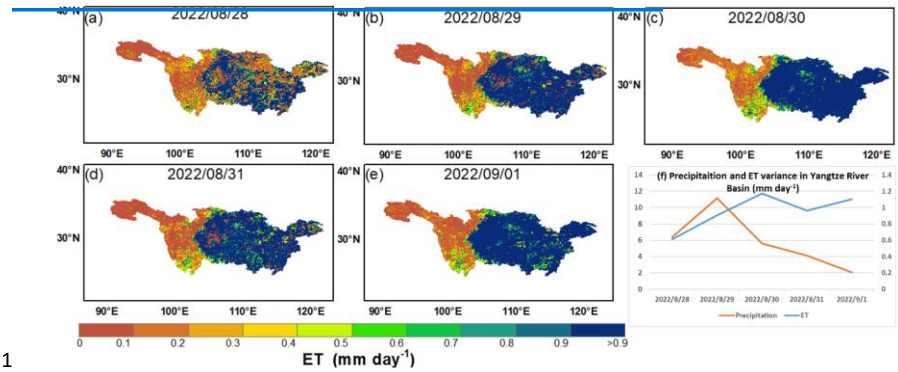


~~**Figure 9.** Daily ET distribution of VISEA from August 28$^{th}$ to September 1$^{st}$ in 2022) (a)-(e) and mean ET and Precipitation Variance in the Yangtze River Basin (f) during the same period.~~

~~In subfigure (f), the variances in mean ET and precipitation across the river basin during this period are showcased. Notably, a substantial increase in rainfall (11 mm day$^{-1}$) on August 29$^{th}$, 2022, was responsible for the surge in ET (1.1 mm day$^{-1}$) on August 30$^{th}$, 2022, indicating an alleviation of drought conditions within the region. The consistent alignment of ET and precipitation variances underlines VISEA's ability to capture near-real-time fluctuations in ET, particularly during drought events.~~

The VISEA ET product demonstrates consistent spatial distribution patterns among the six ET products across various years, both in terms of annual means (a-g) and latitude zonal means (h). These patterns align closely with the precipitation distribution data from GPCC. It also exhibits similar distributions to other ET products, both below the 5$^{th}$ percentile (Figure S4) and above the 95$^{th}$ percentile (Figure S5). The highest ET values (about 1,500 mm year$^{-1}$) are predominantly concentrated in equatorial low-latitude regions with the highest precipitation levels (nearly 2.500 mm year$^{-1}$). The available water for evaporation and transpiration is abundant, and the primary constraint on evapotranspiration lies in the availability of energy to drive the process. In such conditions, water availability is not a limiting factor, allowing for ample potential evapotranspiration. These regions include South America (Amazon Basin), Central Africa (Congo Basin), and Southeast Asia (encompassing Indonesia, Malaysia, parts of Thailand, and the Philippines), which are known for their tropical rainforest climates. These ET estimates align with the findings of Chen et al. (2021) and Zhang et al. (2019) who reported that the multi-year average annual ET is nearly 1,500 and the precipitation is approximately 2,500 mm year$^{-1}$ (Panagos et al., 2017).

Conversely, areas categorized as barren land (BAR), including deserts such as Sahara, Arabian, Gobi, Kalahari, and large portions of Australia, as well as snow and ice (SI) areas like most parts of Canada, Russia, and the Qinghai-Tibet Plateau in China, where the growing seasons are short, typically falling below 400 mm year$^{-1}$. These areas are also characterized by the lowest annual precipitation, ranging from 200 to 400 mm year$^{-1}$ according to GPCC precipitation data mm year$^{-1}$. ET estimates for other land cover types fall within this range, varying from 400 to 1,400 mm year$^{-1}$, in close alignment with the GPCC precipitation data, which falls between 600 to 1,600 mm year$^{-1}$. In these areas, there is a surplus of available energy, and the primary limitation on ET stems from the availability of water. This implies a high atmospheric water demand, often quantified as potential evapotranspiration (potential ET).

In regions with moisture-limited evapotranspiration (ET), the primary constraint on ET arises from the limited availability of water. These areas typically experience insufficient precipitation or water supply, leading to a situation where the atmospheric demand for moisture exceeds the available water resources. On the other hand, regions with energy-limited ET face limitations due to inadequate energy for the process of evaporation and transpiration. This can be influenced by factors such as cloud cover, shading, or other conditions that limit the absorption of solar radiation. In such areas, even if there is an ample water supply, the lack of sufficient energy hinders the rate of evapotranspiration.

Regarding the inter-annual monthly variations, panel (i) shows the fluctuations in ET across different years for the analyzed ET products and precipitation data. The graph reveals a rhythmic pattern of ET across the years, VISEA with other ET products showed distinctive peaks and troughs that correspond to seasonal changes and inter-annual climate variability. The ET products' data exhibit a close alignment with the precipitation patterns reported by GPCC, highlighting the interconnectedness between ET and precipitation as climatic variables. Notably, FLUXCOM consistently presents higher ET estimations compared to the other products, and GLEAM's ET estimations are also slightly higher during the winter, indicating a trend of systematic overestimation in these products relative to the others in the dataset.

Figure 9 presents the daily variations in ET from VISEA and GLEAM along with the precipitation from Global Unified Gauge-Based Analysis of Daily Precipitation recorded in the Yangtze River Basin during from August 26$^{th}$, 2022, to September 2$^{nd}$, 2022. According to a study by Zhang et al. (2023), the Yangtze River Basin endured a significant drought during the summer of 2022, beginning in July and showing signs of abatement towards the end of August and into early September. As GLEAM failed to capture the variability of ET during this drought and exhibited a negative correlation with precipitation data from CPC, we wouldn't discuss it further in this context.

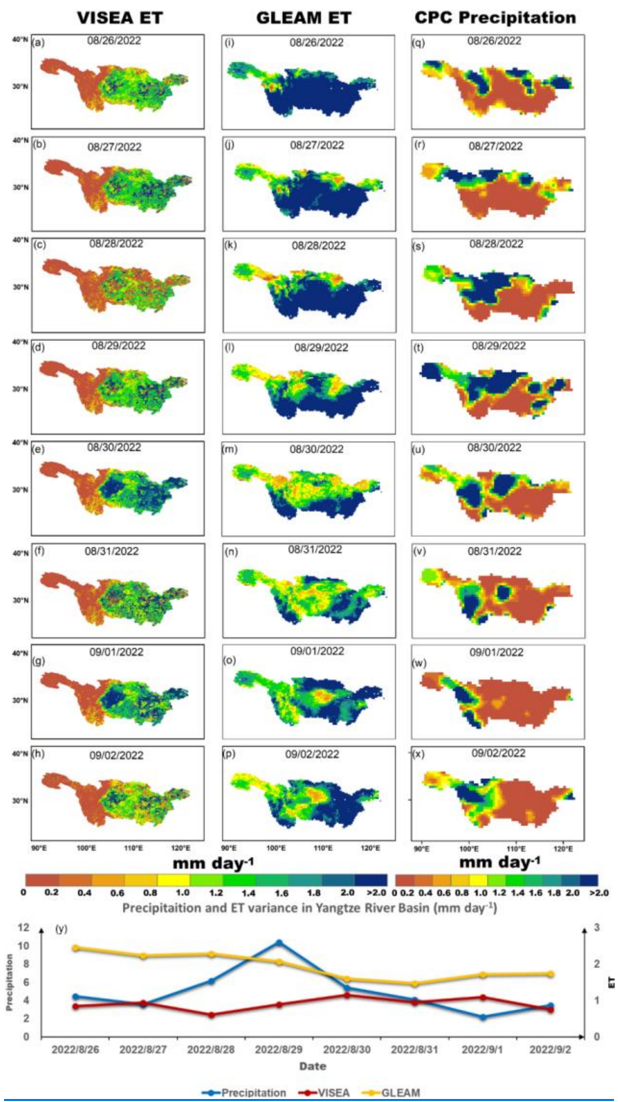


**Figure 9.** Daily ET from VISEA (a-h), GLEAM (i-p), and CPC precipitation (q-x) distributions from August $26^{th}$ to September $2^{nd}$ in 2022, alongside daily mean ET and Precipitation variances in the Yangtze River Basin (y) during the same period.

VISEA ET graphically illustrates the evolving drought conditions: with notably low ET levels (below 1 mm day$^{-1}$) across the basin on August $26^{th}$ to $28^{th}$, evidenced in panel (a-c). A notable increase in precipitation on August $29^{th}$, reflected in panels (s) and (u), correlates with an upswing in ET values (surpassing 1 mm day$^{-1}$) throughout the basin, as visualized in panels (d-f). The graph in panel (y) displays the variances in mean ET and precipitation within the basin over this timeframe, highlighting a significant rise in ET (up to 11 mm day$^{-1}$) on August 30$^{th}$, which corresponds with the observed increase precipitation (reaching 11 mm day$^{-1}$) on August 29$^{th}$.

VISEA's ET data align closely with the variances observed in the CPC precipitation data, showcasing its effectiveness in capturing daily ET fluctuations, especially during and after the drought conditions. It accurately reflects the dip and subsequent recovery in ET values following the precipitation events, indicating its robustness in near-real-time monitoring of ET during such hydrological extremes.

**5. Discussion**

While global ET products require at least 2 weeks (GLEAM, FLUXCOM, AVHRR and PML ET products has more than one years' delay, MOD16 has at least 2 weeks delay) to generate global actual ET ~~measurement~~estimation, we developed VISEA, a satellite-based algorithm which is capable of generating near-real-time evapotranspiration on a daily time step with a resolution of 0.05°. Compared with the monthly global ET of GLEAM, FLUXCOM, AVHRR which have more than two years' delay and 8-day of MOD16 and PML which has more than two weeks' delay and also more than one years' delay. This algorithm is based Nishida et al. (2003) satellite-based evaporation fraction algorithm. To assess its accuracy, we compared the calculated ET with data from 149 flux towers around the world in various land use types.

Scale mismatch is a problem for many satellite-based ET products. The footprints of these flux towers typically range from 100 to 200 meters, while the VISEA model outputs gridded cells at a resolution of 0.05° × 0.05° (nearly 25 km²). This discrepancy introduces errors, especially since flux towers require a uniform fetch, which may not represent the larger gridded cell~~. To enhance the validity of our assessments, we assessed monthly values and spatial patterns of our ET measurements with five other satellite-based ET products named MOD16, AVHRR, GLEAM, GBAF~~ (Sun et al., 2023). To enhance the validity of our assessments, we assessed monthly values and spatial patterns of our ET measurements with five other satellite-based ET products named MOD16, AVHRR, GLEAM, FLUXCOM and PML (Figure 7 and 8).

The evapotranspiration is calculated with VISEA using shortwave downwards radiation, and intermediate variables including daily air temperature and net radiation. The calculated evapotranspiration generally matches local measurements and other model calculated values well but we found significant biases (Figures 6 and 7). These biases largely arise from inaccuracies in the input ERA5-Land shortwave radiation (Figure 3), improper application of the VI-Ts method (Figure 4), and uncertainties in daily net radiation (Figure 5). Below we detail the origin of the biases.

Incoming shortwave radiation from ERA5-Land is employed to derive the available energy for vegetation coverage and bare soil (Eq. ~~20 and 21), which are the main parameters for calculating daily ET (Eq. 22). While ERA5-Land is widely utilized as a reanalysis dataset, offering near-real-time land variables by integrating model data with global observations based on physical laws. However, the accuracy of shortwave radiation from ERA5-Land seems compromised in savannas (Figure 3) due to the challenges associated with simulating radiation transmission under land-use changes and aerosol~~

~~pollution from natural or anthropogenic sources.~~14 and 15), which are the main parameters for calculating daily ET (Eq. 16). While ERA5-Land is widely utilized as a reanalysis dataset, offering near-real-time land variables by integrating model data with global observations based on physical laws. However, the accuracy of shortwave radiation from ERA5-Land seems compromised in savannas (Figure 3) due to the challenges associated with simulating radiation transmission under land-use changes and aerosol pollution from natural or anthropogenic sources (Babar et al., 2019; Martens et al., 2020).

~~Air temperature is an important parameter in determining the daily evaporation fraction of bare soil (Eq. 14), canopy surface resistance (Eq. A1), aerodynamic resistance of the bare soil (Eq. A9), atmospheric emissivity (B1), available energy for vegetation coverage and bare soil (Eq. 20 and 21). Since air temperature is not measured directly by satellites, many other ET product use therefore ground observations, land model or reanalysis data. In contrast, VISEA derives the air temperature from the negative linear relationship between vegetation index (VI) and surface temperature (Ts) using the VI-Ts method (section 2.1.3). It gives very good results under grass land, open shrubland and woody savannas landcover types, as shown in Figure 4. However, in regions where the vegetation index and temperature data in adjacent grid cells show small variations, such as dense forests and bare lands and deserts. Also, in regions with freezing temperatures, the VI-$T_s$ method does perform well, because warmer temperature is related to increased vegetation, opposite the other regions, where there is a negative.~~

~~Another source of bias stems from our VISEA model, is the daily net radiation's uncertainties. which are primarily attributed to the input shortwave radiation and air temperature, as indicated by the energy budget equation (Eq. 17).~~

~~The ET calculation in VISEA relies solely on vegetation coverage~~ Air temperature is an important parameter in determining the daily evaporation fraction of bare soil (Appendix B), canopy surface resistance, aerodynamic resistance of the bare soil (Appendix D) and atmospheric emissivity (Appendix E), available energy for vegetation coverage and bare soil (Eq. 14 and 15). Since air temperature is not measured directly by satellites, many other ET product use therefore ground observations, land model or reanalysis data. In contrast, VISEA derives the air temperature from the negative linear relationship between vegetation index (VI) and surface temperature (Ts) using the VI-Ts method (section 2.1.3). It gives very good results under grass land, open shrubland and woody savannas landcover types, as shown in Figure 4. As previously explained, the VI-Ts method relies on the negative linear correlation between the Vegetation Index (VI) and surface temperature (Ts) within a 5 × 5 grid. Therefore, both the variance of VI values across these grid cells and the negative correlation are essential for calculating the air temperature (Nishida et al., 2003). However, in regions where the vegetation index and temperature data in adjacent grid cells show small variations, such as dense forests and bare lands and deserts. Also, in regions with freezing temperatures, the VI-$T_S$ method does perform well, because warmer temperature is related to increased vegetation, opposite the other regions, where there is a positive correlation between the vegetation index and surface temperature (Cui et al., 2021).

Another bias source of the VISEA model is the uncertainties of daily net radiation, notably originating from input downward shortwave radiation from ERA5-Land (Figure 2) and VI-Ts estimated air temperature (Figure 4). The energy budget equation (Eq. 11) and these two figures indicate that net radiation shows more uncertainties than shortwave radiation and air temperature. At the same time, assuming a linear relationship between cloud coverage (Eq. 12 and 13) and the calculation of downwards longwave radiation (Eq. 14 and 15) may be an oversimplification that could introduce uncertainties. Since available energy for evapotranspiration (ET) depends on net radiation (Eq. 16), addressing these uncertainties is crucial for enhancing overall model accuracy (Brutsaert, 1975; Huang et al., 2023). Future refinements will contribute to a more precise daily net radiation estimation within the VISEA model.

The VISEA model calculates ET primarily based on vegetation coverage, utilizing it as an indirect constraint ~~and~~to estimate evapotranspiration. However, this model does not ~~explicitly account for~~ directly incorporate variables related to water availability~~. This approach overestimates evapotranspiration (ET)~~, which is a critical factor in ET processes. In tropical regions~~ with excessively high~~ , where there is an abundance of solar radiation (available energy~~. Additionally, VISEA~~), the model tends to overestimate ET due to its emphasis on vegetation coverage without adequately accounting for the actual water available for evapotranspiration. This methodology, while effective in capturing the influence of vegetation on ET under varied conditions, can lead to overestimations in areas where energy availability significantly exceeds water availability, typical of many tropical regions. Our analysis and subsequent discussion aim to highlight this characteristic of the VISEA model, acknowledging its implications for ET estimations in such energy-rich, water-variable environments.

Furthermore, the VISEA model exhibits a tendency to underestimate ET in colder ~~areas~~regions within the 60°N to 90°N latitude range, such as the western ~~regions~~territories of Canada~~, which is attributed~~. This underestimation is primarily due to the model's ~~failure~~inability to ~~account for~~incorporate evaporation from frozen surfaces ~~in~~into its ET calculations. These discrepancies arise from several factors: inaccuracies in the ERA5-Land shortwave radiation data (illustrated in Figure 3), the misapplication of the VI-Ts method (explained in Figure 4), and the uncertainties in daily net radiation (depicted in Figure 5). Designed to amalgamate bare soil and full vegetation coverage as depicted in Equation 1, the VISEA model encounters difficulties in accurately estimating ET at higher latitudes, especially in conditions of reduced solar radiation. These challenges are predominantly linked to the uncertainties associated with ERA5-Land shortwave radiation data, further compounded by increased cloudiness levels in these regions, as highlighted by Babar et al. (2019). Such uncertainties have a substantial impact on the model's performance at higher latitudes, affecting its reliability in these conditions.

设置了格式: 英语(美国)
设置了格式: 英语(美国)
设置了格式: 英语(美国)
设置了格式: 英语(美国)
设置了格式: 英语(美国)
设置了格式: 英语(美国)
设置了格式: 英语(美国)
设置了格式: 英语(美国)

~~In our efforts to enhance the model, we are planning to refine the model's treatment of frozen surfaces and bare lands, aiming to improve accuracy in colder and arid regions. Future works include improvements that need to be made to reduce the bias in ET, refine the VI-TS method, explore additional factors like aerosols and land use changes, and enhance spatial resolution.~~

Despite these challenges, our analysis confirms the VISEA model's ability to provide valuable ET estimates during the growing season, evidenced by a high Nash-Sutcliffe efficiency (NSE) of 0.4 and a correlation coefficient (R) of 0.9 when compared against local measurements. These findings support the model's applicability for ET estimation in the 60°N to 90°N latitude range, highlighting its effectiveness and relevance during the vegetative growth period.

We recognize that variations in the temporal coverage of ET products can introduce variability into our comparisons. To mitigate this, we have deliberately chosen validation datasets spanning from 2001 to 2020, achieving a uniform analysis timeframe. This selection enabled us to utilize a diverse range of ET products, effectively minimizing the influence of temporal discrepancies on our comparative analysis. Concentrating on this two-decade interval has allowed us to robustly evaluate spatial and inter-annual ET variability, significantly reducing potential biases associated with differing dataset durations. This method enhances the clarity of our validation approach, solidifies the reliability of our comparisons, and ensures our analysis accurately reflects long-term ET dynamics.

The VISEA ET product provides near-real-time global evapotranspiration (ET) data with a mere one-week delay and a daily resolution of 0.05 degrees, making it a valuable asset for the research community. It empowers researchers by providing access to information on land surface water consumption in near-real-time, which is crucial for monitoring and predicting droughts, and enables decision-makers to make well-informed choices. This not only enhances research efficiency but also supports more effective and expedited actions within the scientific and environmental research community.

The accuracy of the VISEA model could be enhanced by incorporating additional satellite and climate data with higher resolution and improved accuracy. Moreover, the delay in providing ET data could be reduced to three days or less by integrating real-time updated satellite and climate data. In response to the suggestion to conclude our discussion with specific recommendations for future research directions, we recognize the importance of addressing the identified gaps and uncertainties. We propose exploring the development of alternative methods for estimating air temperature and net radiation to provide more accurate and reliable models. Additionally, incorporating variables such as soil moisture and water availability into the model could further refine its precision. By integrating these suggestions, we aim to outline a comprehensive roadmap for future research that builds upon our findings, significantly contributing to the enhancement of environmental modelling and prediction within the field.

## 6. Conclusion

In recent decades, several ET products using satellites have been developed, but few of them provide near-real-time global terrestrial ET estimates. Despite being updated at the fastest rate, the MOD16 ET dataset still encounters a delay of more than two weeks. In this study, we provide a satellite-based near-real-time global daily terrestrial ET estimates by incorporating near-real-time updated hourly shortwave radiation data from ERA5 and MODIS land products at a spatial resolution of 0.05°. The assessments indicate that near-real-time ET estimation with VISEA achieves comparable accuracy to other existing data products and offers a significantly shorter time frame for daily data availability.

The new VISEA aligns well with measurements at 149 tower flux sites distributed globally in both daily and monthly time scales. It ~~exhibits superior accuracy compared to the other five ET products for~~

~~DNF land cover types and~~ demonstrates competitive ~~accuracy for~~correlation coefficients and Nash-Sutcliffe efficiencies (NSEs) across most land cover types but exhibits higher biases. However, like the other five ET products, it encounters greater uncertainties for the SAV land cover type. In the comparison of the multiple-year average spatial distribution of other monthly ET products and GPCC precipitation, VISEA ~~aligns with GPCC and other ET estimates in most areas worldwide, indicating its adherence to the water balance in those regions.~~consistently demonstrates spatial patterns aligned with GPCC in most areas, featuring elevated values in tropical rainforest regions and lower values in arid and semi-arid zones. This alignment underscores VISEA's proficiency in portraying the spatial distribution of evapotranspiration, offering valuable insights into water consumption dynamics across diverse geographical regions. However, VISEA exhibits slightly higher estimates in the Sahara region and lower estimations in the western Canada. In future studies, the VISA ET algorithm can be enhanced by incorporating more precise models for the radiation estimation in savanna and the evaporation from the frozen surface. These improvements will greatly contribute to enhancing the overall accuracy of the algorithm. The satellite-based near-real-time global daily terrestrial ET estimates could be beneficial for meteorology and hydrology applications requiring real-time data, especially in coordinating relief efforts during droughts.

## 7. Code Availability

Python code to synthesise the results and to generate the figures of VISEA results and the codes for generating the global ET products can be obtained through the public repository at https://doi.org/10.6084/m9.figshare.24647721.v1 (Huang, 2023c).

## 8. Data Availability

The VISEA ET data can be obtained from https://data.tpdc.ac.cn/en/data/236e33bf-e66b-4682-bbc1-274de1dcbcd3 ~~(Huang, 2023a)~~(Huang, 2023a).

### 8.1 Input data

MOD11C1 can be obtained at https://e4ftl01.cr.usgs.gov/MOLT/MOD11C1.061/. MOD09CMG can be obtained at https://e4ftl01.cr.usgs.gov/MOLT/MOD09CMG.061/. MCD43C3 can be obtained at https://e4ftl01.cr.usgs.gov/MOTA/MCD43C3.061/. MOD13C1 can be obtained at https://e4ftl01.cr.usgs.gov/MOLT/MOD13C1.061/. MCD12C1 can be obtained at https://e4ftl01.cr.usgs.gov/MOLT/MOD21C1.061/. ERA5-Land shortwave radiation data can be obtained at https://cds.climate.copernicus.eu/cdsapp#!/dataset/reanalysis-era5-land?tab=form.

### 8.2 Evaluation data

FLUXNET2015 flux towers data (FLUXNET2015: CC-BY-4.0 33) can be obtained at https://fluxnet.org/data/download-data/. The GLEAM 3.8a ET dataset was obtained from https://www.gleam.eu/#downloads (an email is required to receive a password for the SFTP). The ~~GBAF~~FLUXCOM ET dataset was ~~acquired~~freely available (CC4.0 BY licence) from https://www.~~bgc-~~

~~jena.mpg.de/geodb/projects/~~fluxcom.org/EF-Download/ the Data~~.php.~~ Portal (an email is required to are receive a password for the FTP). MOD16 ET with the resolution of 0.05° was ~~obtained~~freely downloaded from http://files.ntsg.umt.edu/data/NTSG_Products/MOD16/MOD16A2_MONTHLY.MERRA_GMAO_1kmALB/Previous/. Additionally, the AVHRR ET dataset with 1° was sourced from http://files.ntsg.umt.edu/data/ET_global_monthly_ORIG/Global_1DegResolution/ASCIIFormat/. Lastly, the PML ET dataset was obtained from https://www.tpdc.ac.cn/zh-hans/data/48c16a8d-d307-4973-abab 972e9449627c.

The precipitation from Global Precipitation Climatology Centre (GPCC) data was as obtained at https://cds.climate.copernicus.eu/cdsapp#!/dataset/insitu-gridded-observations-global-and-regional?tab=form. The precipitation from Global Unified Gauge-Based Analysis of Daily Precipitation (CPC) was obtained at https://downloads.psl.noaa.gov/Datasets/cpc_global_precip/precip.2022.nc

Other data that supports the analysis and conclusions of this work is available at https://figshare.com/articles/dataset/Satellite-based_Near-Real Time_Global_Daily_Terrestrial_Evapotranspiration_Estimates/24669306 ~~(Huang, 2023d)~~(Huang, 2023d).

## Appendix

**Appendix A.** **Determining the vegetation fraction calculation:**

$$f_{veg} = \frac{NDVI - NDVI_{min}}{NDVI_{max} - NDVI_{min}} \quad \text{(A1)}$$

where the $NDVI$ is the Normalized Difference Vegetation Index and can be calculated as:

$$NDVI = \frac{R_{nir} - R_{red}}{R_{nir} + R_{red}} \quad \text{(A2)}$$

where $NDVI_{min}$ is the $NDVI$ of the bare soil without plants and $NDVI_{max}$ is the $NDVI$ of the full vegetation cover, $R_{nir}$ is the near-infrared reflectance and $R_{red}$ is the red reflectance. The daily reflectance $R_{nir}$ and $R_{red}$ were measured by MODIS reflectance data MOD09CMG (Fig. 1). Based on Tang et al. (2009), we set $NDVI_{min} = 0.22$ and $NDVI_{max} = 0.83$. Missing observation for the daily MOD09CMG calculated $NDVI$ data was filled with the 16-day averaged $NDVI$ values in the MOD13Q1data product (Fig. 1).

## Appendix B. Determining the instantaneous EF:

Combining Eq. 1 and 4, we fist calculated the instantaneous evaporation fraction, $EF^i$ as:

$$EF^i = f_{veg}\frac{Q_{veg}^i}{Q^i}\,EF_{veg}^i + (1-f_{veg})\frac{Q_{soil}^i}{Q^i}\,EF_{soil}^i \qquad \text{(B1)}$$

where the superscript $i$ stands for the instantaneous value of the parameter, $EF_{veg}^i$ and $EF_{soil}^i$ are the instantaneous full vegetation coverage and bare soil $EF$, respectively. $EF_{veg}^i$ can be expressed as a function of instantaneously parameters as ( Nishida et al., 2003):

$$EF_{veg}^i = \frac{\alpha\,\Delta^i}{\Delta^i+\gamma(1+r_{c\,veg}^i/2r_{a\,veg}^i)} \qquad \text{(B2)}$$

where α is the Priestley-Taylor parameter, which was set to 1.26 for wet surfaces (De Bruin, 1983); $\Delta^i$ is the slope of the saturated vapor pressure, which is a function of the temperature (Pa K$^{-1}$); $\gamma$ is the psychometric constant (Pa K$^{-1}$); $r_{c\,veg}^i$ is the instantaneous surface resistance of the vegetation canopy (s m$^{-1}$); $r_{a\,veg}^i$ is the instantaneous aerodynamics resistance of the vegetation canopy (s m$^{-1}$). $EF_{soil}^i$ was expressed by Nishida et al. (2003) as a function of the instantaneous soil temperature and the available energy based on the energy budget of the bare soil:

$$EF_{soil}^i = \frac{T_{soil\,max}^i - T_{soil}^i}{T_{soil\,max}^i - T_a^i}\,\frac{Q_{soil0}^i}{Q_{soil}^i} \qquad \text{(B3)}$$

where $T_{soil\,max}^i$ is the instantaneous maximum possible temperature at the surface reached when the land surface is dry (K), $T_{soil}^i$ is the instantaneous temperature of the bare soil (K), $T_a^i$ is the instantaneous air temperature, $Q_{soil0}^i$ is the instantaneous available energy when $T_{soil}^i$ is equal to $T_a^i$ (W m$^{-2}$).

**带格式的:** 段落间距段后: 1 行

**Appendix C. Determining of decoupling factor:**

$\Omega_i^*$ is the value of the decoupling factor, $\Omega$, for wet surface. According to Pereira (2004), $\Omega$ and $\Omega^*$ can be expressed as:

$$\Omega = \frac{1}{1+\frac{\gamma}{\Delta+\gamma}\frac{r_c}{r_a}} \tag{C1}$$

$$\Omega^* = \frac{1}{1+\frac{\gamma}{\Delta+\gamma}\frac{r^*}{r_a}} \tag{C2}$$

$$r^* = \frac{(\Delta+\gamma)\rho C_p VPD}{\Delta\gamma(R_n-G)} \tag{C3}$$

where $r_c$ is the surface resistance (s m$^{-1}$); $r_a$ is the aerodynamic resistance (s m$^{-1}$); the calculation details of instantaneous and daily $r_c$ and $r_a$ for vegetation and soil are explained in Appendix A. $r^*$ is the critical surface resistance when the actual evapotranspiration equals the potential evaporation (called equilibrium evapotranspiration, s m$^{-1}$); $\rho$ is the air density (kg m$^{-3}$); $C_p$ is the specific heat of the air (J kg$^{-1}$ K$^{-1}$); $VPD$ is the vapor pressure deficit of the air (Pa). $\Delta$ is the slope of the saturated vapor pressure (Pa K$^{-1}$).

**Appendix D. Determining the resistances of vegetation canopy and bare soil surface**

The canopy surface resistance of the vegetation, denoted as $r_{c\ veg}$ (s m$^{-1}$), was determined using the relationship established by Jarvis et al. ~~(1976)~~(1976), is equivalent to:

$$\frac{1}{r_{c\ veg}} = \frac{f_1(T_a) f_2(PAR) f_3(VPD) f_4(\varphi) f_5(co_2)}{r_{cMIN}} + \frac{1}{r_{cuticle}} \qquad (\cancel{A1}D1)$$

~~The minimum resistance $r_{cMIN}$ (s m$^{-1}$) is defined as 33 (s m$^{-1}$) for cropland and 50 (s m$^{-1}$) for forest as determined by Tang et al. (2009); the canopy resistance related to diffusion through the cuticle layer of leaves $r_{cuticle}$ is set at 100,000 (s m$^{-1}$) in the Biome-BGC model is according to White et al. (2000). The relationships involving air temperature $T_a$, $f_1(T_a)$ and photosynthetic active radiation $PAR$, $f_2(PAR)$ expressed by the functions provided Jarvis et al. (1976):~~

$$\cancel{f_1(T_a) = \left(\frac{T_a - T_n}{T_o - T_n}\right)\left(\frac{T_x - T_a}{T_x - T_a}\right)^{\left(\frac{T_x - T_o}{T_o - T_n}\right)} \qquad (A2)}$$

The minimum resistance $r_{cMIN}$ (s m$^{-1}$) is defined as 33 (s m$^{-1}$) for cropland and 50 (s m$^{-1}$) for forest as determined by Tang et al. (2009); the canopy resistance related to diffusion through the cuticle layer of leaves $r_{cuticle}$ is set at 100,000 (s m$^{-1}$) in the Biome-BGC model is according to White et al. (2000). The relationships involving air temperature $T_a$, $f_1(T_a)$ and photosynthetic active radiation $PAR$, $f_2(PAR)$ expressed by the functions provided Jarvis et al. (1976):

$$f_1(T_a) = \left(\frac{T_a - T_n}{T_o - T_n}\right)\left(\frac{T_x - T_a}{T_x - T_a}\right)^{\left(\frac{T_x - T_o}{T_o - T_n}\right)} \qquad (D2)$$

The minimum, optimal, and maximum temperatures for stomatal activity are denoted as $T_n$, $T_o$ and $T_x$, respectively. As per Tang et al. (2009), $T_n$ is set to 275.85 K, $T_o$ to 304.25 K, and $T_x$ to 318.45 K. The expression for the function $f_2(PAR)$ is provided below:

$$f_2(PAR) = \frac{PAR}{PAR + A} \qquad (\cancel{A3}D3)$$

where $PAR$ is photosynthetic active radiation per unit area and time (μ mol m$^{-2}$ s$^{-1}$) calculated by incoming solar radiation multiplied by 2.05 (White et al., 2000); $A$ is a parameter related to photon absorption efficiency at low light intensity, which was set to 152 μ mol m$^{-2}$ s$^{-1}$ 20; Nishida[32] found that in Eq. ~~A1~~D1 the following functions can be omitted without great loss of accuracy: the functions depending on vapor pressure deficit, $f_3(VPD)$, leaf water potential $f_4(\varphi)$ and carbon dioxide vapor pressure, $f_5(CO_2)$.

The photosynthetic active radiation per unit area and time ($PAR$), measured in μ mol m⁻² s⁻¹, is computed by multiplying incoming solar radiation by 2.05, as outlined by White et al. ~~(2000). The parameter A, associated with photon absorption efficiency at low light intensity, is established at 152 μ mol m⁻² s⁻¹. Nishida et al. (2003) observed that, in Eq. A1, the functions tied to vapor pressure deficit~~

~~$f_3$ ($VPD$), leaf water potential $f_4$ ($\varphi$), and carbon dioxide vapor pressure $f_5$ ($CO_2$) can be omitted without significant loss of accuracy~~(2000). The parameter A, associated with photon absorption efficiency at low light intensity, is established at 152 µ mol m$^{-2}$ s$^{-1}$. Nishida et al. (2003) observed that, in Eq. D1, the functions tied to vapor pressure deficit $f_3$ ($VPD$), leaf water potential $f_4$ ($\varphi$), and carbon dioxide vapor pressure $f_5$ ($CO_2$) can be omitted without significant loss of accuracy. Tang et al. (2009) employed this canopy resistance approach to estimate evapotranspiration (ET) at a 500 meter resolution in the Kalam river basin. The evaluation of their results indicated that the simplification of these calculations did not significantly impact the final accuracy of ET estimates. Additionally, Huang et al. (2017, 2021, and 2023) evaluated this method for 0.05 degree ET assessments across China. The evaluation results also demonstrated that the reduction in vapor pressure deficit (VPD) and leaf water potential had minimal effects on the final ET estimates.

The aerodynamic resistance of the canopy, denoted as $r_{a\,veg}$ (s m$^{-1}$), is computed for forest cover, grassland, and cropland using the empirical formulae presented by Nishida et al. (2003) for both instantaneous and daily values.

$$\frac{1}{r_{a\,veg\,(forest)}} = 0.008U_{50m} \qquad (\cancel{A4}D4)$$

The wind speed at a height of 50 meters above the canopy ($U_{50m}$) is used to determine the aerodynamic resistance for grassland and cropland, as follows:

$$\frac{1}{r_{a\,veg\,(grassland\,\&\,cropland)}} = 0.003U_{1m} \qquad (\cancel{A5}D5)$$

where $U_{1m}$ is the wind speed 1m above the canopy (m s$^{-1}$). The wind speed as a function of the height z, $U(z)$ can be calculated by the logarithm profile of wind. A recent study found that the velocity log law does not apply to a stratified atmospheric boundary layer (Cheng et al., 2011). Thus ~~A4~~D4 and ~~A5~~D5 are valid under neutral boundary layer conditions. Since $r_{a\,veg}$ is calculated differently for forests (Eq. ~~A4~~D4) and grasslands/croplands (Eq. ~~A5~~D5), we used the land cover classes from the yearly International Geosphere-Biosphere Programme (IGBP) (MCD12C1) to identify the land cover and choice the different equation of $r_{a\,veg}$. $U_{50m}$ and $U_{1m}$ were calculated by the logarithm profile of wind:

$$U(z) = U_{shear}\ln\left[\frac{(z-d)}{z_0}\right]/k \qquad (\cancel{A6}D6)$$

where $U_{shear}$ is the shear velocity (m s$^{-1}$); $z$ is the height (m); $d$ is the surface displacement (m); $z_0$ is the roughness length, we followed Nishida et al. (2003), set as 0.005 m for bare soil and 0.01 m for grassland; $k$ is the von Kármán's constant and set as 0.4 following Nishida (Nishida et al., 2003). The shear velocity $U_{shear}$ was calculated as:

$$U_{shear} = U_{1m\,soil}\,\frac{0.4}{\ln\left(\frac{1}{0.005}\right)} \qquad (\cancel{A7}D7)$$

where the $U_{1m\,soil}$ is the wind speed of bare soil at 1 m height (m s$^{-1}$), it was calculated as:

$$U_{1m\,soil} = 1/0.0015\, r_{a\,soil}$$ (~~A8~~D8)

The Vegetation Index-surface Temperature (VI-$T_S$) diagram (Nishida et al., 2003) can be utilized to compute the instantaneous air temperature. This is achieved by utilizing MODIS instantaneous surface temperature/emissivity data (MOD11C1) and daily-calculated NDVI as input parameters.

The aerodynamic resistance of the bare soil, denoted as $r_{a\,soil}$ (s $m^{-1}$), was determined by Nishida et al. (2003). This calculation assumes that the maximum surface temperature of bare soil $T_{soil\,max}$ (K) happens when the sum of latent heat flux and sensible heat flux of the bare soil, referred to as the available energy of bare soil $Q_{soil}$ (W $m^{-2}$), is utilized as the sensible heat flux, while the latent heat flux is set to zero.

$$r_{a\,soil} = \frac{\rho C_p (T_{soil\,max} - T_a)}{Q_{soil}}$$ (~~A9~~D9)

$r_{a\,soil}$ is the aerodynamic resistance of the bare soil, (s $m^{-1}$), $\rho$ is the air density, kg $m^{-3}$; $C_p$ is the specific heat of the air, (J $kg^{-1}$ $K^{-1}$); $T_a$ is the air temperature (K), $Q_{soil}$ is the available energy of bare soil (W $m^{-2}$).

To compute the canopy surface resistance of bare soil, denoted as $r_{c\,soil}$ (s $m^{-1}$), we adhere to the methodologies outlined in the works of Griend and Owe (1994) and Mu et al. (2007):

$$r_{c\,soil} = r_{tot} - r_{a\,soil}$$ (~~A10~~D10)

$$r_{tot} = \frac{1.0}{\left(\frac{T_a}{293.15}\right)^{1.75} \frac{101300}{P}} * 107.0$$ (~~A11~~D11)

The total aerodynamic resistance $r_{tot}$ (s $m^{-1}$) is composed of the aerodynamic resistance over the bare soil $r_{a\,soil}$ (s $m^{-1}$), with atmospheric pressure $P$ set at 101,300 Pa.

**Appendix ~~B~~E. The calculation of atmospheric emissivity for clear sky**

As per Brutsaert (1975), the atmospheric emissivity $\varepsilon_a^d$ for clear sky under standard humidity and temperature conditions is

$$\varepsilon_a^d = 1.24 \times (e_a^d / T_a^d)^{1/7} \qquad (\text{~~B1~~E1})$$

where $e_a^d$ represents the daily water vapor pressure (kPa). To calculated $e_a^d$, it is necessary to compute the slope of the saturated vapor (Δ) as:

$$\Delta = \frac{4098\,[0.6108\,\exp[\frac{17.27T_a}{(T_a+237.3)}]]}{(T_a+237.3)^2} \qquad (\text{~~B2~~E2})$$

VPD is the vapor pressure deficit of the air (kPa), which is expressed as:

$$\mathrm{VPD} = e^0(T_a) - e_a \qquad (\text{~~B3~~E3})$$

$$e^0(T_a) = 0.6108\,\exp\,[\frac{17.27T_a}{(T_a+237.3)}] \qquad (\text{~~B4~~E4})$$

$$e_a = e^0(T_{dew}) \qquad (\text{~~B5~~E5})$$

$$e^0(T_{dew}) = 0.6108\,\exp\,[\frac{17.27T_{dew}}{T_{dew}+237.3}] \qquad (\text{~~B6~~E6})$$

The expression within parentheses denotes the independent variable, where, $e^0(T_a)$ represents the saturation vapor pressure (kPa) at the air temperature $T_a$ (℃); $e_a$ is the actual vapor pressure (kPa); $e^0(T_{dew})$ is the saturation vapor pressure (kPa) at the dew point temperature $T_{dew}$ (℃). For forest, water surface, and cropland $T_{dew}$ is set to the minimum air temperature during the day. In arid regions such as bare soil and non-irrigated grassland, $T_{dew}$ may be 2-3 ℃ lower than $T_{min}$. Therefore, 2 ℃ is subtracted is subtracted from $T_{min}$ in arid and semiarid areas to derive $T_{dew}$. While these simplifications might introduce a bias in the final calculated ET value, our initial results indicate that the effect is negligible.

**Acknowledgements**

This study is supported by the National Key Research and Development Program of China (No.2017YFA0603703). We employed ChatGPT3.5 to enhance the quality of our English writing and grammar.

**Author contributions**

L. H. had the original idea and drafted the paper with help from Y. L.; J. M. C. Q. T., T. S., W. C. and W. S. participated in the discussion and the many manuscript revisions.

**Competing interests**

The authors declare no competing interests.

**References**

Aschonitis, V., Touloumidis, D., ten Veldhuis, M.-C., and Coenders-Gerrits, M.: Correcting Thornthwaite potential evapotranspiration using a global grid of local coefficients to support temperature-based estimations of reference evapotranspiration and aridity indices, Earth System Science Data, 14, 163–177, https://doi.org/10.5194/essd-14-163-2022, 2022.

Awada, H., Di Prima, S., Sirca, C., Giadrossich, F., Marras, S., Spano, D., and Pirastru, M.: A remote sensing and modeling integrated approach for constructing continuous time series of daily actual evapotranspiration, Agricultural Water Management, 260, 107320, https://doi.org/10.1016/j.agwat.2021.107320, 2022.

Babar, B., Graversen, R., and Boström, T.: Solar radiation estimation at high latitudes: Assessment of the CMSAF databases, ASR and ERA5, Solar Energy, 182, 397–411, https://doi.org/10.1016/j.solener.2019.02.058, 2019.

Baldocchi, D., Falge, E., Gu, L., Olson, R., Hollinger, D., Running, S., Anthoni, P., Bernhofer, C., Davis, K., Evans, R., Fuentes, J., Goldstein, A., Katul, G., Law, B., Lee, X., Malhi, Y., Meyers, T., Munger, W., Oechel, W., U, K. T. P., Pilegaard, K., Schmid, H. P., Valentini, R., Verma, S., Vesala, T., Wilson, K., and Wofsy, S.: FLUXNET: A New Tool to Study the Temporal and Spatial Variability of Ecosystem-Scale Carbon Dioxide, Water Vapor, and Energy Flux Densities, Bulletin of the American Meteorological Society, 82, 2415–2434, https://doi.org/10.1175/1520-0477(2001)082<2415:FANTTS>2.3.CO;2, 2001.

Barrios, J. M., Ghilain, N., Arboleda, A., and Gellens-Meulenberghs, F.: Retrieving daily evapotranspiration from the combination of geostationary and polar-orbit satellite data, in: 2015 8th International Workshop on the Analysis of Multitemporal Remote Sensing Images (Multi-Temp), 2015 8th International Workshop on the Analysis of Multitemporal Remote Sensing Images (Multi-Temp), 1–4, https://doi.org/10.1109/Multi-Temp.2015.7245797, 2015.

Becker, A., Finger, P., Meyer-Christoffer, A., Rudolf, B., Schamm, K., Schneider, U., and Ziese, M.: A description of the global land-surface precipitation data products of the Global Precipitation Climatology Centre with sample applications including centennial (trend) analysis from 1901–present, Earth System Science Data, 5, 71–99, https://doi.org/10.5194/essd-5-71-2013, 2013.

Brutsaert, W.: On a derivable formula for ~~longwave~~long-wave radiation from clear skies, Water Resources Research, 11, 742–744, https://doi.org/10.1029/WR011i005p00742, 1975.

Chang, K. and Zhang, Q.: Modeling of downward longwave radiation and radiative cooling potential in China, Journal of Renewable and Sustainable Energy, 11, 066501, https://doi.org/10.1063/1.5117319, 2019.

Chen, X., Su, Z., Ma, Y., Trigo, I., and Gentine, P.: Remote Sensing of Global Daily Evapotranspiration based on a Surface Energy Balance Method and Reanalysis Data, Journal of Geophysical Research: Atmospheres, 126, e2020JD032873, https://doi.org/10.1029/2020JD032873, 2021.

Cheng, L., Xu, Z., Wang, D., and Cai, X.: Assessing interannual variability of evapotranspiration at the catchment scale using satellite-based evapotranspiration data sets, Water Resources Research, 47, https://doi.org/10.1029/2011WR010636, 2011.

Copernicus Climate Change Service: Crop productivity and evapotranspiration indicators from 2000 to present derived from satellite observations, https://doi.org/10.24381/CDS.B2F6F9F6, 2020.

Cui, Y., Jia, L., and Fan, W.: Estimation of actual evapotranspiration and its components in an irrigated area by integrating the Shuttleworth-Wallace and surface temperature-vegetation index schemes using the particle swarm optimization algorithm, Agricultural and Forest Meteorology, 307, 108488, https://doi.org/10.1016/j.agrformet.2021.108488, 2021.

De Bruin, H. a. R.: A Model for the Priestley-Taylor Parameter α, J. Climate Appl. Meteor., 22, 572–578, https://doi.org/10.1175/1520-0450(1983)022<0572:AMFTPT>2.0.CO;2, 1983.

Didan, K.: MOD13C1 MODIS/Terra Vegetation Indices 16-Day L3 Global 0.05Deg CMG V006 [~~data~~Data set], https://doi.org/10.5067/MODIS/MOD13C1.006, n.d.

Fisher, J. B., Lee, B., Purdy, A. J., Halverson, G. H., Dohlen, M. B., Cawse-Nicholson, K., Wang, A., Anderson, R. G., Aragon, B., Arain, M. A., Baldocchi, D. D., Baker, J. M., Barral, H., Bernacchi, C. J., Bernhofer, C., Biraud, S. C., Bohrer, G., Brunsell, N., Cappelaere, B., Castro-Contreras, S., Chun, J., Conrad, B. J., Cremonese, E., Demarty, J., Desai, A. R., De Ligne, A., Foltýnová, L., Goulden, M. L., Griffis, T. J., Grünwald, T., Johnson, M. S., Kang, M., Kelbe, D., Kowalska, N., Lim, J.-H., Maïnassara, I., McCabe, M. F., Missik, J. E. C., Mohanty, B. P., Moore, C. E., Morillas, L., Morrison, R., Munger, J. W., Posse, G., Richardson, A. D., Russell, E. S., Ryu, Y., Sanchez-Azofeifa, A., Schmidt, M., Schwartz, E., Sharp, I., Šigut, L., Tang, Y., Hulley, G., Anderson, M., Hain, C., French, A., Wood, E., and Hook, S.: ECOSTRESS: NASA's Next Generation Mission to Measure Evapotranspiration From the International Space Station, Water Resources Research, 56, e2019WR026058, https://doi.org/10.1029/2019WR026058, 2020.

Friedl, M., D. Sulla-Menashe.: MCD12C1 MODIS/Terra+Aqua Land Cover Type Yearly L3 Global 0.05Deg CMG V006 [~~data~~Data set], https://doi.org/10.5067/MODIS/MCD12C1.006, 2015.

Fritschen, L. J. and Gay, L. W.: Soil Heat Flux, in: Environmental Instrumentation, edited by: Fritschen, L. J. and Gay, L. W., Springer, New York, NY, 86–92, https://doi.org/10.1007/978-1-4612-6205-3_4, 1979.

Goforth, M. A., Gilchrist, G. W., and Sirianni, J. D.: Cloud effects on thermal downwelling sky radiance, in: Thermosense XXIV, 203–213, https://doi.org/10.1117/12.459570, 2002.

Griend, A. A. van de and Owe, M.: Bare soil surface resistance to evaporation by vapor diffusion under semiarid conditions, Water Resources Research, 30, 181–188, https://doi.org/10.1029/93WR02747, 1994.

Halverson, G. H., Fisher, J., Jewell, L. A., Moore, G., Verma, M., McDonald, T., Kim, S., and Muniz, A.: Near Real-Time Monitoring of Global Evapotranspiration and its Application to Water Resource Management, 2016, H54D-01, 2016.

Han, C., Ma, Y., Wang, B., Zhong, L., Ma, W., Chen, X., and Su, Z.: Long-term variations in actual evapotranspiration over the Tibetan Plateau, Earth System Science Data, 13, 3513–3524, https://doi.org/10.5194/essd-13-3513-2021, 2021.

He, S., Zhang, Y., Ma, N., Tian, J., Kong, D., and Liu, C.: A daily and 500 m coupled evapotranspiration and gross primary production product across China during 2000–2020, Earth System Science Data, 14, 5463–5488, https://doi.org/10.5194/essd-14-5463-2022, 2022.

Huang, L.: Satellite-based Near-Real-Time Global Terrestrial Evapotranspiration Estimation ~~National Tibetan Plateau / Third Pole Environment Data Center [data set],~~Dataset, https://doi.org/. https://doi.org/10.11888/Terre.tpdc.300782_. https://cstr.cn/18406.11.Terre.tpdc.300782~~., 2023a~~ ., 2023.

~~Huang, L., Luo, Y., Steenhuis, T., Tang, Q., Cheng, W., Shi, W., Xia, X., Zhao, D., and Liao, Z.: An Improved Satellite-Based Evapotranspiration Procedure for China, Earth and Space Science, 10, e2023EA002949, https://doi.org/10.1029/2023EA002949, 2023b.~~

~~Huang, L., Satellite-based Near-Real-Time Global Daily Terrestrial Evapotranspiration Estimates. figshare. [Software]. https://doi.org/10.6084/m9.figshare.24647721.v1,2023c.~~

~~Huang, L.: Satellite-based Near-Real-Time Global Daily Terrestrial Evapotranspiration Estimates. figshare [data set], https://doi.org/10.6084/m9.figshare.24669306.v1, 2023d.~~

Huang, L., Li, Z., Tang, Q., Zhang, X., Liu, X., and Cui, H.: Evaluation of satellite-based evapotranspiration estimates in China, JARS, 11, 026019, https://doi.org/10.1117/1.JRS.11.026019, 2017.

Huang, L., Steenhuis, T. S., Luo, Y., Tang, Q., Tang, R., Zheng, J., Shi, W., and Qiao, C.: Revisiting Daily MODIS Evapotranspiration Algorithm Using Flux Tower Measurements in China, Earth and Space Science, 8, e2021EA001818, https://doi.org/10.1029/2021EA001818, 2021.

Huang, L., Luo, Y., Steenhuis, T., Tang, Q., Cheng, W., Shi, W., Xia, X., Zhao, D., and Liao, Z.: An Improved Satellite-Based Evapotranspiration Procedure for China, Earth and Space Science, 10, e2023EA002949, https://doi.org/10.1029/2023EA002949, 2023.

Idso, S. B., Aase, J. K., and Jackson, R. D.: Net radiation — soil heat flux relations as influenced by soil water content variations, Boundary-Layer Meteorol, 9, 113–122, https://doi.org/10.1007/BF00232257, 1975.

Jarvis, P. G., Monteith, J. L., and Weatherley, P. E.: The interpretation of the variations in leaf water potential and stomatal conductance found in canopies in the field, Philosophical Transactions of the Royal Society of London. B, Biological Sciences, 273, 593–610, https://doi.org/10.1098/rstb.1976.0035, 1976.

Jiang, H., Yang, Y., Bai, Y., and Wang, H.: Evaluation of the Total, Direct, and Diffuse Solar Radiations From the ERA5 Reanalysis Data in China, IEEE Geoscience and Remote Sensing Letters, 17, 47–51, https://doi.org/10.1109/LGRS.2019.2916410, 2020.

Jung, M.: FLUXCOM Global Land Energy Fluxes,~~ [data set],~~ https://doi.org/10.17871/FLUXCOM_EnergyFluxes_v1, 2018.

Jung, M., Reichstein, M., and Bondeau, A.: Towards global empirical upscaling of FLUXNET eddy covariance observations: validation of a model tree ensemble approach using a biosphere model, Biogeosciences, 6, 2001–2013, https://doi.org/10.5194/bg-6-2001-2009, 2009.

Jung, M., Reichstein, M., Ciais, P., Seneviratne, S. I., Sheffield, J., Goulden, M. L., Bonan, G., Cescatti, A., Chen, J., de Jeu, R., Dolman, A. J., Eugster, W., Gerten, D., Gianelle, D., Gobron, N., Heinke, J., Kimball, J., Law, B. E., Montagnani, L., Mu, Q., Mueller, B., Oleson, K., Papale, D., Richardson, A. D., Roupsard, O., Running, S., Tomelleri, E., Viovy, N., Weber, U., Williams, C., Wood, E., Zaehle, S., and Zhang, K.: Recent decline in the global land evapotranspiration trend due to limited moisture supply, Nature, 467, 951–954, https://doi.org/10.1038/nature09396, 2010.

Jung, M., Koirala, S., Weber, U., Ichii, K., Gans, F., Camps-Valls, G., Papale, D., Schwalm, C., Tramontana, G., and Reichstein, M.: The FLUXCOM ensemble of global land-atmosphere energy fluxes, Sci Data, 6, 1–14, https://doi.org/10.1038/s41597-019-0076-8, 2019.

Kondo Junsei: Atmospheric Science near the Ground Surface, University of Tokyo Press, Tokyo, 324 pp., 2000.

Martens, B., Miralles, D. G., Lievens, H., van der Schalie, R., de Jeu, R. A. M., Fernández-Prieto, D., Beck, H. E., Dorigo, W. A., and Verhoest, N. E. C.: GLEAM v3: satellite-based land evaporation and root-zone soil moisture, Geoscientific Model Development, 10, 1903–1925, https://doi.org/10.5194/gmd-10-1903-2017, 2017.

Martens, B., Schumacher, D. L., Wouters, H., Muñoz-Sabater, J., Verhoest, N. E. C., and Miralles, D. G.: Evaluating the land-surface energy partitioning in ERA5, Geoscientific Model Development, 13, 4159–4181, https://doi.org/10.5194/gmd-13-4159-2020, 2020.

Martin Jung, Sujan Koirala, Ulrich Weber, Kazuhito Ichii, Fabian Gans, Gustau Camps-Valls, Dario Papale, Christopher Schwalm, Gianluca tramontana & Markus Reichstein: FLUXCOM Global Land Energy Fluxes, https://doi.org/10.17871/ FLUXCOM_EnergyFluxes_v1, 2018.

Miralles, D. G., Holmes, T. R. H., De Jeu, R. a. M., Gash, J. H., Meesters, A. G. C. A., and Dolman, A. J.: Global land-surface evaporation estimated from satellite-based observations, Hydrology and Earth System Sciences, 15, 453–469, https://doi.org/10.5194/hess-15-453-2011, 2011.

Mu, Q., Heinsch, F. A., Zhao, M., and Running, S. W.: Development of a global evapotranspiration algorithm based on MODIS and global meteorology data, Remote Sensing of Environment, 111, 519–536, https://doi.org/10.1016/j.rse.2007.04.015, 2007.

Mu, Q., Zhao, M., and Running, S. W.: Improvements to a MODIS global terrestrial evapotranspiration algorithm, Remote Sensing of Environment, 115, 1781–1800, https://doi.org/10.1016/j.rse.2011.02.019, 2011.

Mu, Q., Zhao, M., Kimball, J. S., McDowell, N. G., and Running, S. W.: A Remotely Sensed Global Terrestrial Drought Severity Index, Bulletin of the American Meteorological Society, 94, 83–98, https://doi.org/10.1175/BAMS-D-11-00213.1, 2013.

Muñoz Sabater, J.: ERA5-Land hourly data from 1950 to present., https://doi.org/DOI: 10.24381/cds.e2161bac, 2019.

Naud, C. M., Booth, J. F., and Genio, A. D. D.: Evaluation of ERA-Interim and MERRA Cloudiness in the Southern Ocean, Journal of Climate, 27, 2109–2124, https://doi.org/10.1175/JCLI-D-13-00432.1, 2014.

Nishida, K., Nemani, R. R., Running, S. W., and Glassy, J. M.: An operational remote sensing algorithm of land surface evaporation, Journal of Geophysical Research: Atmospheres, 108, https://doi.org/10.1029/2002JD002062, 2003.

Panagos, P., Borrelli, P., Meusburger, K., Yu, B., Klik, A., Yang, J., Ni, J., Chattopadhyay, N., Sadeghi, S. H., Hazbavi, Z., Zabihi, M., Larionov, G., Krasnov, S., Gorobets, A., Levi, Y., Erpul, G., Birkel, C., and Ballabio, C.: Global rainfall erosivity assessment based on high-temporal resolution rainfall records, Scientific Reports, 7, https://doi.org/10.1038/s41598-017-04282-8, 2017.

Pastorello, G., Trotta, C., Canfora, E., Chu, H., Christianson, D., Cheah, Y.-W., Poindexter, C., Chen, J., Elbashandy, A., Humphrey, M., Isaac, P., Polidori, D., Reichstein, M., Ribeca, A., van Ingen, C., Vuichard, N., Zhang, L., Amiro, B., Ammann, C., Arain, M. A., Ardö, J., Arkebauer, T., Arndt, S. K., Arriga, N., Aubinet, M., Aurela, M., Baldocchi, D., Barr, A., Beamesderfer, E., Marchesini, L. B., Bergeron, O., Beringer, J., Bernhofer, C., Berveiller, D., Billesbach, D., Black, T. A., Blanken, P. D., Bohrer, G., Boike, J., Bolstad, P. V., Bonal, D., Bonnefond, J.-M., Bowling, D. R., Bracho, R., Brodeur, J., Brümmer, C., Buchmann, N., Burban, B., Burns, S. P., Buysse, P., Cale, P., Cavagna, M., Cellier, P., Chen, S., Chini, I., Christensen, T. R., Cleverly, J., Collalti, A., Consalvo, C., Cook, B. D., Cook, D., Coursolle, C., Cremonese, E., Curtis, P. S., D'Andrea, E., da Rocha, H., Dai, X., Davis, K. J., Cinti, B. D., Grandcourt, A. de, Ligne, A. D., De Oliveira, R. C., Delpierre, N., Desai, A. R., Di Bella, C. M., Tommasi, P. di, Dolman, H., Domingo, F., Dong, G., Dore, S., Duce, P., Dufrêne, E., Dunn, A., Dušek, J., Eamus, D., Eichelmann, U., ElKhidir, H. A. M., Eugster, W., Ewenz, C. M., Ewers, B., Famulari, D., Fares, S., Feigenwinter, I., Feitz, A., Fensholt, R., Filippa, G., Fischer, M., Frank, J., Galvagno, M., et al.: The FLUXNET2015 dataset and the ONEFlux processing pipeline for eddy covariance data, Sci Data, 7, 225, https://doi.org/10.1038/s41597-020-0534-3, 2020.

Pereira, A. R.: The Priestley–Taylor parameter and the decoupling factor for estimating reference evapotranspiration, Agricultural and Forest Meteorology, 125, 305–313, https://doi.org/10.1016/j.agrformet.2004.04.002, 2004.

Schaaf, C., Wang, Z: MCD43C1 MODIS/Terra+Aqua BRDF/AlbedoModel Parameters Daily L3 Global 0.05Deg CMG V006 [~~data~~Data set], https://doi.org/10.5067/MODIS/MCD43C1.006, 2015.

Schneider, U., Becker, A., Finger, P., Meyer-Christoffer, A., Ziese, M., and Rudolf, B.: GPCC's new land surface precipitation climatology based on quality-controlled in situ data and its role in quantifying the global water cycle, Theor Appl Climatol, 115, 15–40, https://doi.org/10.1007/s00704-013-0860-x, 2014.

Schneider, U., Finger, P., Meyer-Christoffer, A., Rustemeier, E., Ziese, M., and Becker, A.: Evaluating the Hydrological Cycle over Land Using the Newly-Corrected Precipitation Climatology from the Global Precipitation Climatology Centre (GPCC), Atmosphere, 8, 52, https://doi.org/10.3390/atmos8030052, 2017.

~~Software/model code: Huang, L.: Satellite-based Near-Real-Time Global Daily Terrestrial Evapotranspiration Estimates, figshare [code], https://doi.org/10.6084/m9.figshare.24647721.v1, 2023.~~

Su, B., Huang, J., Mondal, S. K., Zhai, J., Wang, Y., Wen, S., Gao, M., Lv, Y., Jiang, S., Jiang, T., and Li, A.: Insight from CMIP6 SSP-RCP scenarios for future drought characteristics in China, Atmospheric Research, 105375, https://doi.org/10.1016/j.atmosres.2020.105375, 2020.

Sun, S., Bi, Z., Xiao, J., Liu, Y., Sun, G., Ju, W., Liu, C., Mu, M., Li, J., Zhou, Y., Li, X., Liu, Y., and Chen, H.: A global 5 km monthly potential evapotranspiration dataset (1982–2015) estimated by the Shuttleworth-Wallace model, Earth System Science Data Discussions, 1–45, https://doi.org/10.5194/essd-2023-38, 2023.

Tang, Q., Peterson, S., Cuenca, R. H., Hagimoto, Y., and Lettenmaier, D. P.: Satellite-based near-real-time estimation of irrigated crop water consumption, Journal of Geophysical Research: Atmospheres, 114, https://doi.org/10.1029/2008JD010854, 2009.

Tang, R. and Li, Z.-L.: An improved constant evaporative fraction method for estimating daily evapotranspiration from remotely sensed instantaneous observations, Geophysical Research Letters, 44, 2319–2326, https://doi.org/10.1002/2017GL072621, 2017.

Tang, R., Li, Z.-L., Sun, X., and Bi, Y.: Temporal upscaling of instantaneous evapotranspiration on clear-sky days using the constant reference evaporative fraction method with fixed or variable surface resistances at two cropland sites, Journal of Geophysical Research: Atmospheres, 122, 784–801, https://doi.org/10.1002/2016JD025975, 2017.

~~Tapiador, F. J., Turk, F. J., Petersen, W., Hou, A. Y., García-Ortega, E., Machado, L. A. T., Angelis, C. F., Salio, P., Kidd, C., Huffman, G. J., and de Castro, M.: Global precipitation measurement:~~

~~Methods, datasets and applications, Atmospheric Research, 104–105, 70–97, https://doi.org/10.1016/j.atmosres.2011.10.021, 2012.~~

Taylor, K. E.: Summarizing multiple aspects of model performance in a single diagram, Journal of Geophysical Research: Atmospheres, 106, 7183–7192, https://doi.org/10.1029/2000JD900719, 2001.

Udo; Becker, Andreas; Finger, Peter; Meyer-Christoffer, Anja; Rudolf, Bruno; Ziese, Markus: GPCC Full Data Reanalysis Version 6.0 at 2.5°: Monthly Land-Surface Precipitation from Rain-Gauges built on GTS-based and Historic Data., https://doi.org/DOI: 10.5676/DWD_GPCC/FD_M_V7_250, 2011.

Vermote, E: MOD09CMG MODIS/Terra Surface Reflectance Daily L3 Global 0.05Deg CMG V006 [~~data~~Data set], https://doi.org/10.5067/MODIS/MOD09CMG.006, 2015.

Wan, Z., Hook, S., Hulley, G: MOD11C1 MODIS/Terra Land Surface Temperature/Emissivity Daily L3 Global 0.05Deg CMG V006 [~~data~~Data set], https://doi.org/10.5067/MODIS/MOD11C1.006, 2015.

~~Wang, K. and Dickinson, R. E.: Global atmospheric downward longwave radiation at the surface from ground-based observations, satellite retrievals, and reanalyses, Reviews of Geophysics, 51, 150–185, https://doi.org/10.1002/rog.20009, 2013.~~

Wang, K., Ma, Q., Wang, X., and Wild, M.: Urban impacts on mean and trend of surface incident solar radiation, Geophysical Research Letters, 41, 4664–4668, https://doi.org/10.1002/2014GL060201, 2014.

Wang, L., Liu, H., Chen, D., Zhang, P., Leavitt, S., Liu, Y., Fang, C., Sun, C., Cai, Q., Gui, Z., Liang, B., Shi, L., Liu, F., Zheng, Y., and Grießinger, J.: The 1820s Marks a Shift to Hotter-Drier Summers in Western Europe Since 1360, Geophysical Research Letters, 49, e2022GL099692, https://doi.org/10.1029/2022GL099692, 2022.

Wang, R., Gentine, P., Yin, J., Chen, L., Chen, J., and Li, L.: Long-term relative decline in evapotranspiration with increasing runoff on fractional land surfaces, Hydrology and Earth System Sciences, 25, 3805–3818, https://doi.org/10.5194/hess-25-3805-2021, 2021a.

Wang, Y., Zhao, X., Mamtimin, A., Sayit, H., Abulizi, S., Maturdi, A., Yang, F., Huo, W., Zhou, C., Yang, X., and Liu, X.: Evaluation of Reanalysis Datasets for Solar Radiation with In Situ Observations at a Location over the Gobi Region of Xinjiang, China, Remote Sensing, 13, 4191, https://doi.org/10.3390/rs13214191, ~~2021~~2021b.

White, M. A., Thornton, P. E., Running, S. W., and Nemani, R. R.: Parameterization and Sensitivity Analysis of the BIOME–BGC Terrestrial Ecosystem Model: Net Primary Production Controls, Earth Interactions, 4, 1–85, https://doi.org/10.1175/1087-3562(2000)004<0003:PASAOT>2.0.CO;2, 2000.

Yang, D., Chen, H., and Lei, H.: Analysis of the Diurnal Pattern of Evaporative Fraction and Its Controlling Factors over Croplands in the Northern China, Journal of Integrative Agriculture, 12, 1316–1329, https://doi.org/10.1016/S2095-3119(13)60540-7, 2013.

Yang, R. and Friedl, M. A.: Modeling the effects of three-dimensional vegetation structure on surface radiation and energy balance in boreal forests, Journal of Geophysical Research: Atmospheres, 108, https://doi.org/10.1029/2002JD003109, 2003.

Zhang, C., Long, D., Zhang, Y., Anderson, M. C., Kustas, W. P., and Yang, Y.: A decadal (2008–2017) daily evapotranspiration data set of 1 km spatial resolution and spatial completeness across the North China Plain using TSEB and data fusion, Remote Sensing of Environment, 262, 112519, https://doi.org/10.1016/j.rse.2021.112519, 2021.

Zhang, K., Kimball, J. S., Mu, Q., Jones, L. A., Goetz, S. J., and Running, S. W.: Satellite based analysis of northern ET trends and associated changes in the regional water balance from 1983 to 2005, Journal of Hydrology, 379, 92–110, https://doi.org/10.1016/j.jhydrol.2009.09.047, 2009.

Zhang, K., Kimball, J. S., Nemani, R. R., and Running, S. W.: A continuous satellite-derived global record of land surface evapotranspiration from 1983 to 2006, Water Resources Research, 46, https://doi.org/10.1029/2009WR008800, 2010.

Zhang, K., Kimball, J. S., Nemani, R. R., Running, S. W., Hong, Y., Gourley, J. J., and Yu, Z.: Vegetation Greening and Climate Change Promote Multidecadal Rises of Global Land Evapotranspiration, Sci Rep, 5, 15956, https://doi.org/10.1038/srep15956, 2015.

Zhang, L., Yu, X., Zhou, T., Zhang, W., Hu, S., and Clark, R.: Understanding and Attribution of Extreme Heat and Drought Events in 2022: Current Situation and Future Challenges, Adv. Atmos. Sci., 40, 1941–1951, https://doi.org/10.1007/s00376-023-3171-x, ~~2023~~2023a.

Zhang, X., Huang, A., Dai, Y., Li, W., Gu, C., Yuan, H., Wei, N., Zhang, Y., Qiu, B., and Cai, S.: Influences of 3D Sub-Grid Terrain Radiative Effect on the Performance of CoLM Over Heihe River Basin, Tibetan Plateau, Journal of Advances in Modeling Earth Systems, 14, e2021MS002654, https://doi.org/10.1029/2021MS002654, 2022.

Zhang, Y.: PML_V2 global evapotranspiration and gross primary production (2002.07-2019.08), ~~National Tibetan Plateau / Third Pole Environment Data Center, [data set],~~ https://doi.org/10.11888/Geogra.tpdc.270251, 2022.

Zhang, Y., Kong, D., Gan, R., Chiew, F. H. S., McVicar, T. R., Zhang, Q., and Yang, Y.: Coupled estimation of 500 m and 8-day resolution global evapotranspiration and gross primary production in 2002–2017, Remote Sensing of Environment, 222, 165–182, https://doi.org/10.1016/j.rse.2018.12.031, 2019.

Zhang, Y., Li, C., Chiew, F. H. S., Post, D. A., Zhang, X., Ma, N., Tian, J., Kong, D., Leung, L. R., Yu, Q., Shi, J., and Liu, C.: Southern Hemisphere dominates recent decline in global water availability, Science, 382, 579–584, https://doi.org/10.1126/science.adh0716, 2023b.